ADVANCED MATERIALS
www.advmat.de

Tetrazine-Linked Covalent Organic Frameworks With Acid Sensing and Photocatalytic Activity

*Amin Zadehnazari, Ahmadreza Khosropour, Ataf Ali Altaf, Andrew S. Rosen, and Alireza Abbaspourrad**

The first synthesis and comprehensive characterization of two vinyl tetrazine-linked covalent organic frameworks (COF), TA-COF-1 and TA-COF-2, are reported. These materials exhibit high crystallinity and high specific surface areas of 1323 and 1114 $m^2 g^{-1}$. The COFs demonstrate favorable band positions and narrow band gaps suitable for light-driven applications. These advantages enable TA-COFs to act as reusable metal-free photocatalysts in the arylboronic acids oxidation and light-induced coupling of benzylamines. In addition, these TA-COFs show acid sensing capabilities, exhibiting visible and reversible color changes upon exposure to HCl solution, HCl vapor, and NH_3 vapor. Further, the TA-COFs outperform a wide range of previously reported COF photocathodes. The tetrazine linker in the COF skeleton represents a significant advancement in the field of COF synthesis, enhancing the separation efficiency of charge carriers during the photoreaction and contributing to their photocathodic properties. TA-COFs can also degrade 5-nitro-1,2,4-triazol-3-one (NTO), an insensitive explosive present in industrial wastewater, in 20 min in a sunlight-driven photocatalytic process; thus, revealing dual functionality of the protonated TA-COFs as both photodegradation and Brønsted acid catalysts. This pioneering work opens new avenues for harnessing the potential of the tetrazine linker in COF-based materials, facilitating advances in catalysis, sensing, and other related fields.

1. Introduction

Photocatalysis has emerged as a powerful tool for a wide range of applications, including renewable energy generation, environmental remediation, and organic synthesis.[1] The development of new and highly efficient photocatalysts is crucial to advance the field of photochemistry specifically to make chemical synthesis more efficient and sustainable.[2]

Significant progress has been made in the development of efficient photocatalysts in recent years. One approach is to use semiconducting materials as they can absorb light energy and generate charge carriers that initiate chemical reactions.[3–5] Other approaches involve designing materials with specific structures and compositions that can enhance their photocatalytic properties.[6–8] One of the major challenges in developing efficient photocatalysts is finding materials that are able to absorb light across a broad spectrum and generate high-energy charge carriers with long lifetimes. Covalent organic frameworks (COF), with their high porosity and extremely well-ordered morphology, have recently gained significant attention as a versatile platform for developing new materials with properties covering a wide range of applications.[9,10] COFs have emerged as promising materials for photocatalysis because of their tunability, porosity, and semiconducting electronic properties.[11–13]

In particular, COFs containing reactive nitrogen or basic building blocks have demonstrated significant potential as acid sensors thanks to their ability to undergo structural variations in response to changes in pH.[14–17] COFs can be used to detect the presence of acidic gases, such as hydrochloric acid,[18] nitric oxide,[19] or nitrogen dioxide[20] in the atmosphere. The use of COFs for acid sensing offers several advantages over conventional sensing materials, including being lightweight, recyclable, and having higher sensitivity, selectivity, and durability.[21] Therefore, a highly sensitive and selective COF-based acid sensor has great potential for accurate detection and monitoring of acid levels.

Vinyl-linked COFs (VCOFs) via Knoevenagel condensation reactions introduced by Zhang and co-workers are of particular interest.[22–24] This reaction results in the formation of a highly ordered, crystalline network of conjugated organic molecules that are linked by vinylene groups. In addition, VCOFs have unique electronic and optical properties due to the presence of the conjugated vinylene linkages in their structures.[25] These abilities

A. Zadehnazari, A. Khosropour, A. A. Altaf, A. Abbaspourrad
Department of Food Science
College of Agricultural and Life Sciences
Cornell University
Stocking Hall, Ithaca, NY 14853, USA
E-mail: Alireza@cornell.edu
A. S. Rosen
Department of Materials Science and Engineering
University of California, Berkeley
Berkeley, CA 94720, USA
A. S. Rosen
Materials Science Division
Lawrence Berkeley National Laboratory
Berkeley, CA 94720, USA
The ORCID identification number(s) for the author(s) of this article can be found under https://doi.org/10.1002/adma.202311042

DOI: 10.1002/adma.202311042

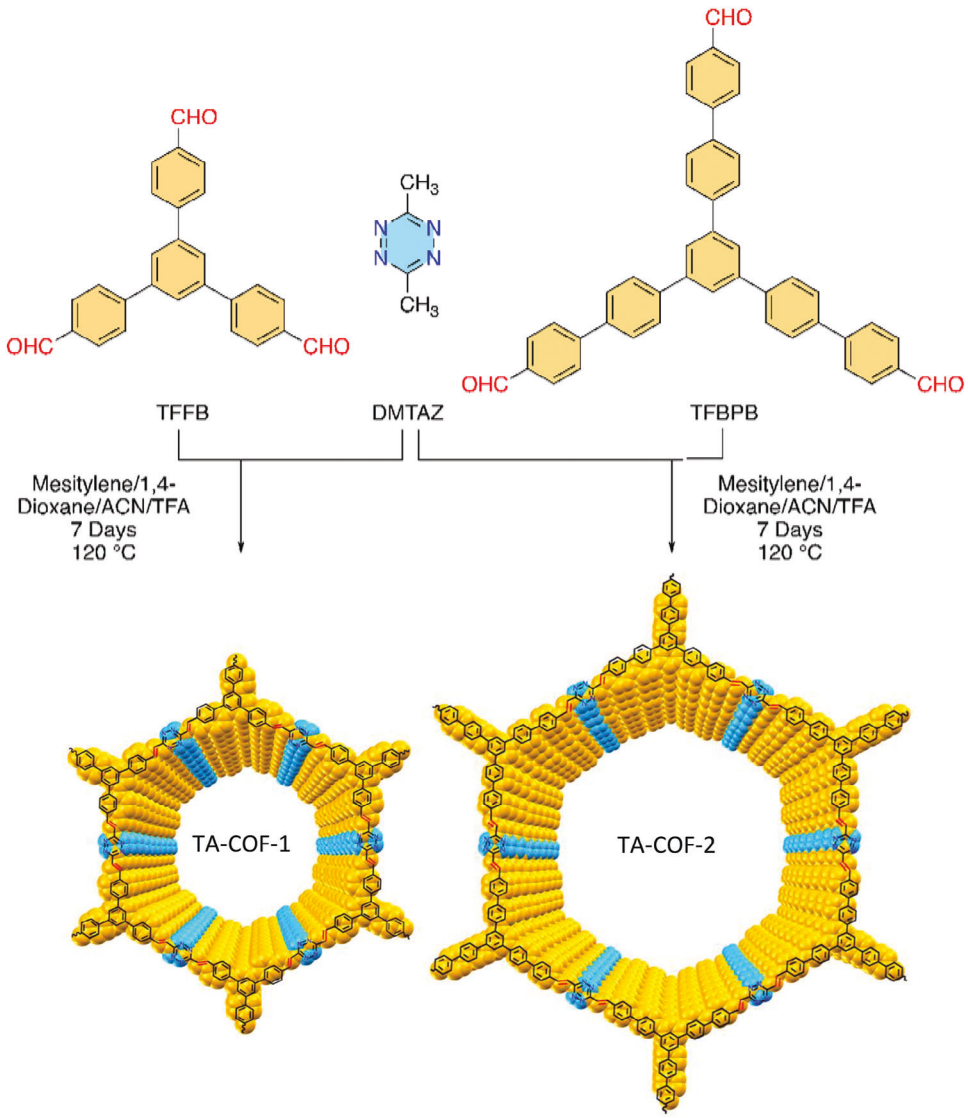

Scheme 1. Synthesis of TA-COF-1 and TA-COF-2 through a Knoevenagel condensation reaction.

make them potentially useful for applications in catalysis,[26] optoelectronics,[27] fuel cell,[28] and energy conversion.[29] One major advantage of VCOFs is their simple synthesis process, along with their flexibility in design. Overall, while all types of COFs offer unique properties and potential applications, the high stability, tunable pore size, and unique electronic and optical properties of VCOFs make them particularly attractive for a wide range of applications. However, the potential and wide variety of structures, features, and applications of VCOFs have only been partially exploited with a relatively small number of investigations reported for VCOFs.[11,30–32,109]

Here, we report the synthesis of a new set of VCOFs using a tetrazine linker that exhibits enhanced properties for acid–base sensing and photocatalyzed oxidation reactions. These vinyl tetrazine-linked COFs (TA-COF-1 and TA-COF-2, **Scheme 1**) were synthesized by the Knoevenagel condensation reaction. The first was made by condensing 3,6-dimethyl-tetrazine (DMTAZ) with 1,3,5-tris(4-formylphenyl)benzene (TFPB) (TA-COF-1) and the second by the same reaction of DMTAZ with 1,3,5-tris(4-formylbiphenyl)benzene (TFBPB) (TA-COF-2). In addition, the challenges that must be addressed and future prospects for TA-COF-based materials for photocatalysis and acid sensing are discussed, aiming to create highly effective TA-COF derivatives for a wide range of applications.

2. Results and Discussion

2.1. Characterization of TA-COF-1 and TA-COF-2

TA-COFs were synthesized via a Knoevenagel condensation reaction using two monomer aldehydes (TFPB) (TA-COF-1) and (TFBPB) (TA-COF-2), both with C_3 symmetry, and a DMTAZ with D_{2h} symmetry as building blocks (Scheme 1). The aldehydes created the corners of the overall hexagonal structure and the tetrazine created the edge linkages. The best solvothermal conditions that resulted in the highest crystallinity

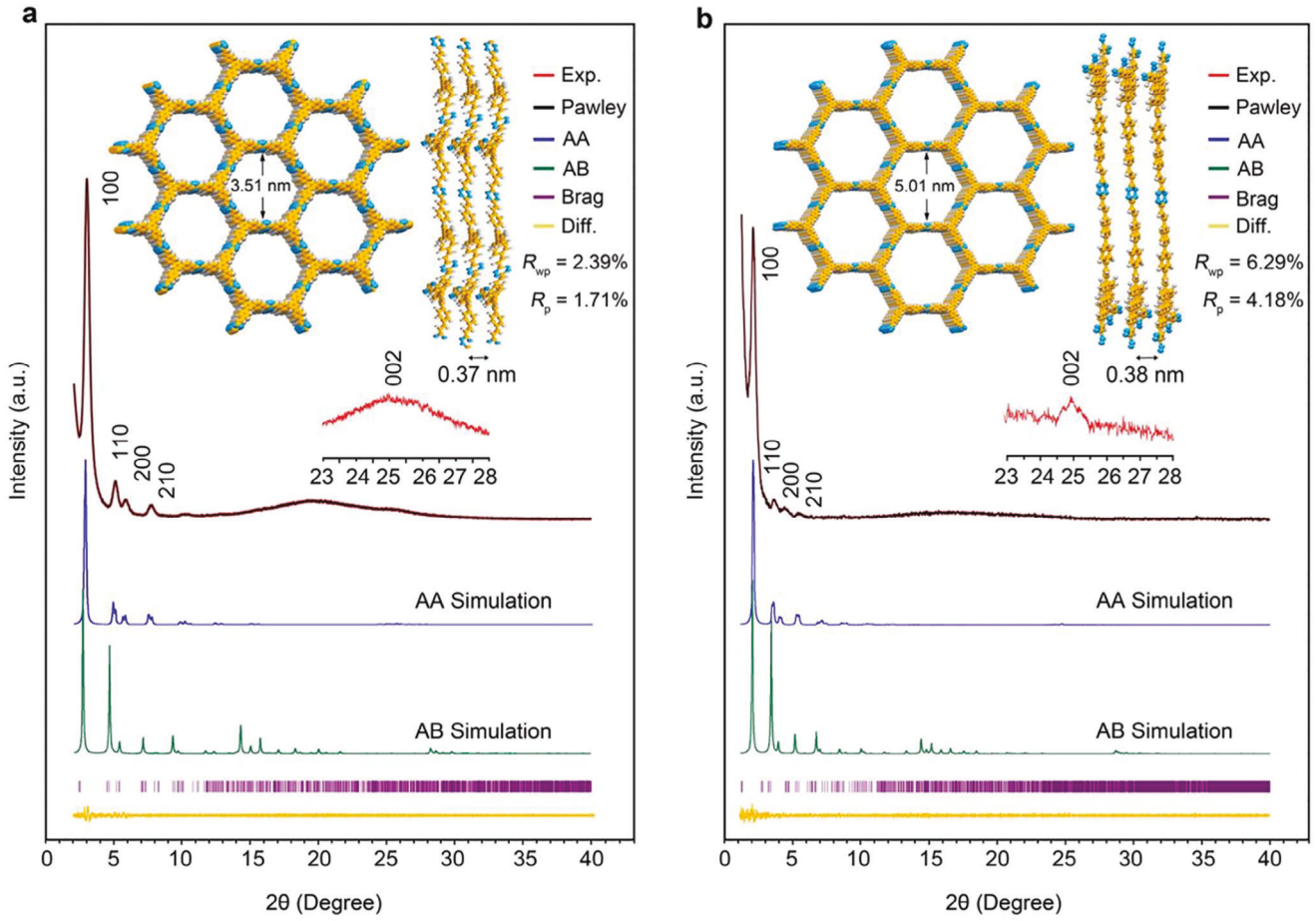

Figure 1. Powder X-ray diffraction patterns of a) TA-COF-1 and b) TA-COF-2: experimentally observed patterns (red), Pawley-refined patterns (black), the simulated patterns for eclipsed AA stacking mode (blue), AB stacking mode (green), the Bragg positions (violet bar), and the refinement difference (yellow). Insets are top (left) and side (right) views of TA-COF-1 and TA-COF-2 with eclipsed (AA) stacking mode from the DFT calculations (orange, carbon; gray, hydrogen; blue, nitrogen).

were found to be a mixed solvent system of mesitylene/1,4-dioxane/acetonitrile/trifluoroacetic acid mixture at 120 °C for 7 days (Table S1, Supporting Information contains other solvent systems explored).

The crystallinity of the TA-COFs was assessed using powder X-ray diffraction (PXRD). The appearance of sharp peaks in the PXRD patterns of both TA-COFs confirmed their high crystallinity. The PXRD spectra of both TA-COFs showed five main Bragg diffraction peaks: for TA-COF-1, the peaks appeared at 2.91°, 4.99°, 5.69°, 7.58°, and 25.34°; and for TA-COF-2, the peaks appeared at 1.98°, 3.42°, 4.18°, 5.27°, and 24.9° (**Figure 1**a,b, red curves). These five peaks were assigned to the (100), (110), (200), (210), and (002) planes. The most intense peak in the PXRD patterns appeared at 2θ = 2.9° for TA-COF-1 and 2θ = 1.98° for TA-COF-2, which corresponds to the (100) plane. The peaks at 2θ = 25.3° for TA-COF-1 and 24.9° for TA-COF-2 in the PXRD patterns were assigned to the (002) plane and are indicative of π–π stacking between the layers. Similar observations have been documented in previously reported COFs,[33–38] wherein all peaks were clearly observed except for the broadening of the 001 peak.

To offer a more definitive confirmation of the AA stacking model in TA-COFs and to achieve a more precise calculation of the interlayer distance between adjacent layers, the diffraction data were collected carefully at a low scan rate in the range of 2θ = 23–28°, and well-resolved peaks were obtained (Figure 1). The interlayer distance between the adjacent sheets was estimated at ≈0.37 and 0.38 nm for TA-COF-1 and TA-COF-2 using the *d* spacing measurement following the Bragg's law.

For TA-COF-1 and TA-COF-2, we first carried out molecular mechanics simulations of proposed AA and AB stacking modes with an initial hexagonal symmetry in space groups *P*6/m and $P6_3$/m, respectively. Based on the Universal Force Field (UFF)[39] results, we predict that the AA stacking mode is more favorable than the AB stacking mode by 20 meV/atom and 23 meV/atom for TA-COF-1 and TA-COF-2, respectively. Using an AA stacking mode, we then performed periodic DFT calculations for TA-COF-1 and TA-COF-2. Depending on the initial atomic configuration, we were able to identify two distinct conformations: a near-perfect planar AA stacking arrangement; and an AA stacking arrangement where each layer was slightly bent (Figures S1 and S2, Supporting Information). Based on the PBE-D3(BJ)[40–42] results, we predict that the bent AA stacking configuration is more stable than the planar AA stacking configuration by 8 meV/atom and 7 meV/atom for TA-COF-1 and TA-COF-2, respectively. This

lower-energy, bent configuration is similar to that reported for other COFs of similar topology[43] and is likely due to increased van der Waals interactions between the layers.

For the planar structures with two layers in the *c* dimension per simulation unit cell, TA-COF-1 and TA-COF-2 are predicted by DFT to have lattice constants of $a = b = 37.48$ Å, $c = 7.37$ Å, $\alpha = \beta = 90.0°$, $\gamma = 120.0°$ and $a = b = 52.54$ Å, $c = 7.41$ Å, $\alpha = \beta = 90.0°$, $\gamma = 120.0°$, respectively. Based on the lower energy bent structures with two layers in the dimension, TA-COF-1 and TA-COF-2 are predicted by DFT to have lattice constants of $a = 37.15$ Å, $b = 37.13$ Å, $c = 7.47$ Å, $\alpha = 101.2°$, $\beta = 97.9°$, $\gamma = 119.3°$ and $a = 52.49$ Å, $b = 52.47$ Å, c = 7.52 Å, $\alpha = 72.6°$, $\beta = 95.0°$, and $\gamma = 120.3°$, respectively. Further application of the models was made for Pawley refinements using the reflex package available in Materials Studio 5.0 software. Very small differences were observed, providing evidence that all of the refined profiles were consistent with the experimentally observed XRD patterns. The Pawley refinement of the PXRD patterns was also in excellent agreement with AA-eclipsed stacking mode (Figure 1a,b, black curves), confirming the PXRD peak assignments and providing exact unit cell values. The unit-cell parameters after refinement were calculated as $a = 37.15 \pm 0.05235$ Å, $b = 36.90 \pm 0.05230$ Å, $c = 7.48 \pm 0.01060$ Å, $\alpha = 101.6 \pm 0.00382°$, $\beta = 97.8 \pm 0.00334°$, and $\gamma = 120.6 \pm 0.00343°$, with $R_{wp} = 2.39\%$ and $R_p = 1.71\%$, for TA-COF-1 and $a = 52.49 \pm 0.05151$ Å, $b = 52.45 \pm 0.05269$ Å, $c = 7.525 \pm 0.01095$ Å, $\alpha = 72.6 \pm 0.00377°$, $\beta = 94.9 \pm 0.00355°$, and $\gamma = 120.3 \pm 0.00398°$, with $R_{wp} = 6.29\%$ and $R_p = 4.18\%$, for TA-COF-2 (All optimized structures and the Pawley-refined result can be found in the Supporting Information).

FT-IR was used to monitor the changes in the functional groups by comparing the COFs to the starting materials. The disappearance of the aldehyde carbonyl group at 1681 cm^{-1} and the appearance of a new C═C bond at 1620 and 1632 cm^{-1} indicated the successful formation of the alkene double bond in the COFs (Figures S3 and S4, Supporting Information) and the C═N and disubstituted *trans* C═C bonds vibrational signals also appeared at 1595 and 969 cm^{-1}.

Solid-state ^{13}C cross-polarization magic-angle spinning (^{13}C CP-MAS) NMR spectroscopy confirmed the presence of the olefin and aromatic carbons as well as the disappearance of the aldehyde groups (**Figure 2**). In the spectra of the TA-COFs, the peak related to the carbon of the tetrazine ring appeared at 167.2 ppm. The spectra had broad peaks in a range between 115 and 146 ppm, which corresponded to their aryl and olefin groups. There was also good consistency between the solid state ^{13}C NMR spectra of TA-COFs and the solution ^{13}C NMR of the model compound BPVT, which was synthesized from the condensation reaction between DMTAZ and BPCA in alcoholic potassium hydroxide (**Scheme 2**).

X-ray photoelectron spectroscopy (XPS) provided detailed information about the surface composition of the TA-COFs (Figures S5a and S6a, Supporting Information). High-resolution XPS spectra of TA-COFs (Figures S5b–d and S6b–d, Supporting Information) showed three different types of carbon environments and two environments for oxygen and nitrogen. For TA-COF-1 (Figure S5a, Supporting Information), the characteristic peak of C 1s was located at 283.2 eV corresponding to the olefin carbon. The peak located at 397.6 was attributed to N 1s from the

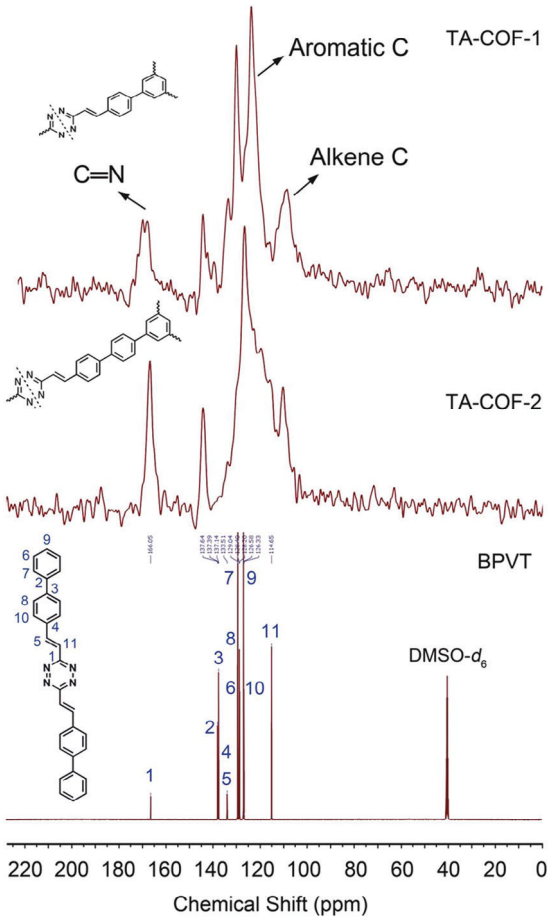

Figure 2. ^{13}C CP-MAS NMR spectra of TA-COF-1 (top) and TA-COF-2 (middle) and solution state ^{13}C NMR spectrum of BPVT (model compound) (bottom) recorded in DMSO-d_6.

tetrazine ring. The spectra also showed a peak at 530.8 eV for O 1s, which was related to the aldehyde end groups present on the edges or defects in the lattice structures of TA-COFs.[44] As expected, the XPS spectra of TA-COF-2 was very similar, with three carbon environments, one nitrogen environment, and a peak at 532.5 eV, indicating the presence of surface aldehyde end groups (Figure S6, Supporting Information).

The porosity of TA-COFs was measured by nitrogen adsorption–desorption experiments, which showed a small hysteresis during the desorption process. The Brunauer–Emmett–Teller (BET) specific surface area was estimated to be 1323 $m^2\ g^{-1}$ for TA-COF-1 and 1114 $m^2\ g^{-1}$ for TA-COF-2, with a total pore volume of 0.278 and 0.216 $cm^3\ g^{-1}$, respectively.

We extended the analysis of nitrogen adsorption isotherms to include the microporous part in the lower relative pressure range (Figure S7, Supporting Information). The micro- and mesopores were characterized using non-local density functional theory (NLDFT) method using the data from the nitrogen adsorption isotherms as a starting point.

Our measurements revealed the presence of micropores in the TA-COFs with pore sizes in the range of nanometer levels, particularly within the 1–5 nm size range (**Figure 3**). The

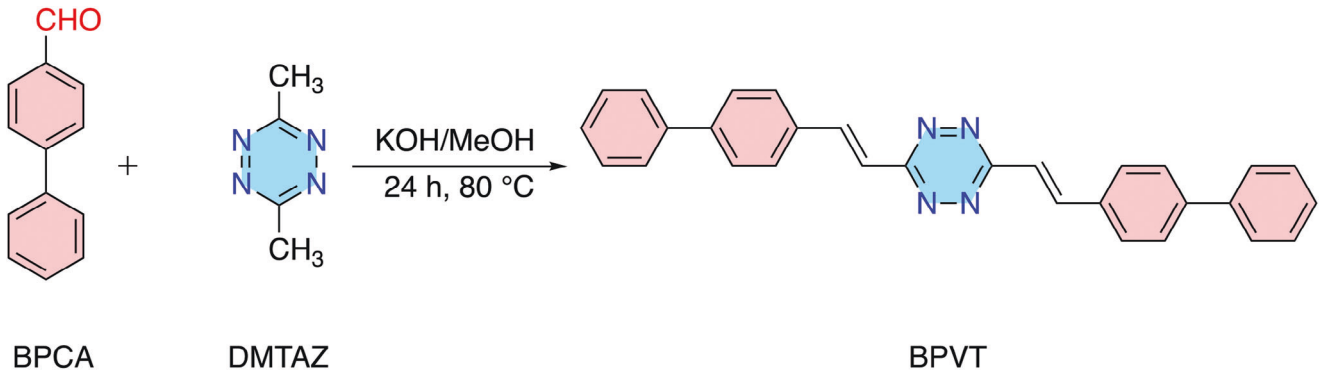

Scheme 2. Synthesis of 3,6-bis((E)-2-([1,1'-biphenyl]-4-yl)vinyl)-1,2,4,5-tetrazine (BPVT).

data from the microporous regions provide crucial insights into the overall porosity and surface area characteristics of the COFs. The results demonstrated a comprehensive picture of the COFs' porosity, encompassing both mesoporous and microporous regions.

The morphology and nanoscopic structure of TA-COFs were imaged using field-emission scanning electron microscopy (FE-SEM) and high-resolution transmission electron microscopy (HRTEM) (**Figure 4**). A highly porous morphology was observed for both TA-COFs in the FE-SEM images (Figure 4a–d). The results showed that TA-COF-1 self-assembled in a flower-shaped morphology while TA-COF-2 had a cluster-like morphology. From the HRTEM images, we observed a well-aligned layered morphology with hexagonal honeycomb-like channels (Figure 4e,f; Figure S8a,b, Supporting Information). The presence of hexagonal pores along the (100) crystal axis validated the AA-stacking mode of the 2D TA-COF structure (Figure 4e, inset; Figure S8a, Supporting Information).

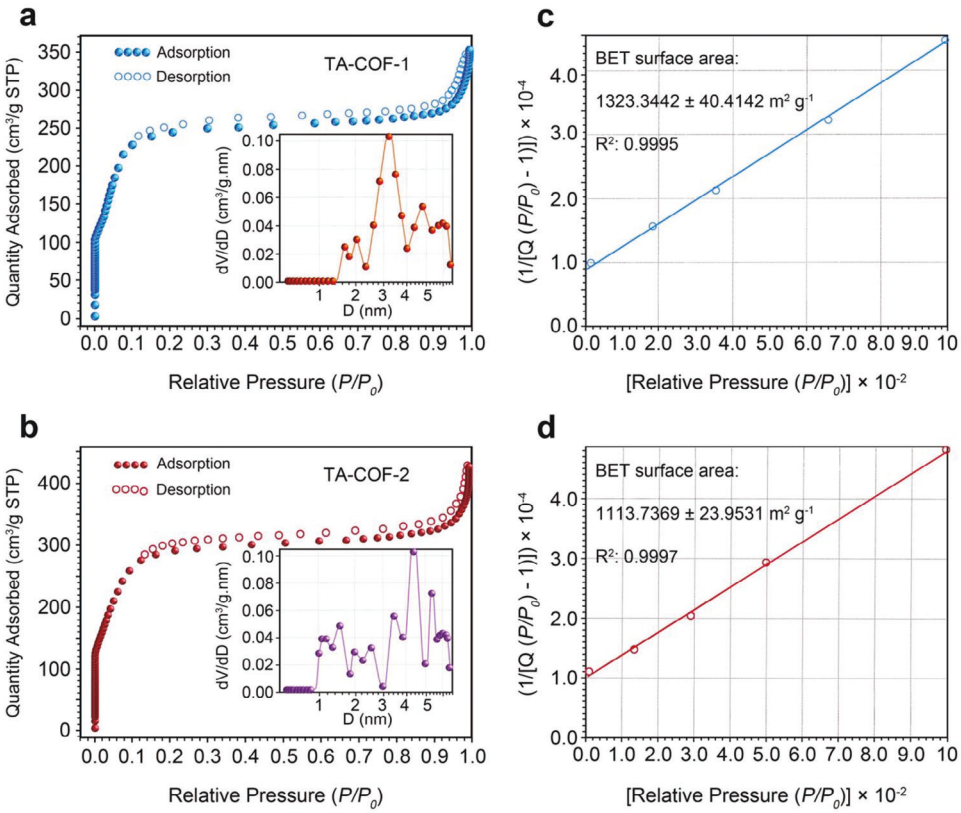

Figure 3. Nitrogen adsorption and desorption isotherms of a) TA-COF-1 and b) TA-COF-2. Adsorption (solid circles) and desorption (open circles), respectively. Inset: Pore size distribution profile of TA-COFs by NLDFT theory on the nitrogen adsorption isotherms. P_0 = saturated vapor pressure of the gas at 77 K, P/P_0 = relative pressure, Va = adsorbed pore volume at standard temperature and pressure, and dV_p = differential pore volume. Multipoint BET fit for c) TA-COF-1 and d) TA-COF-2.

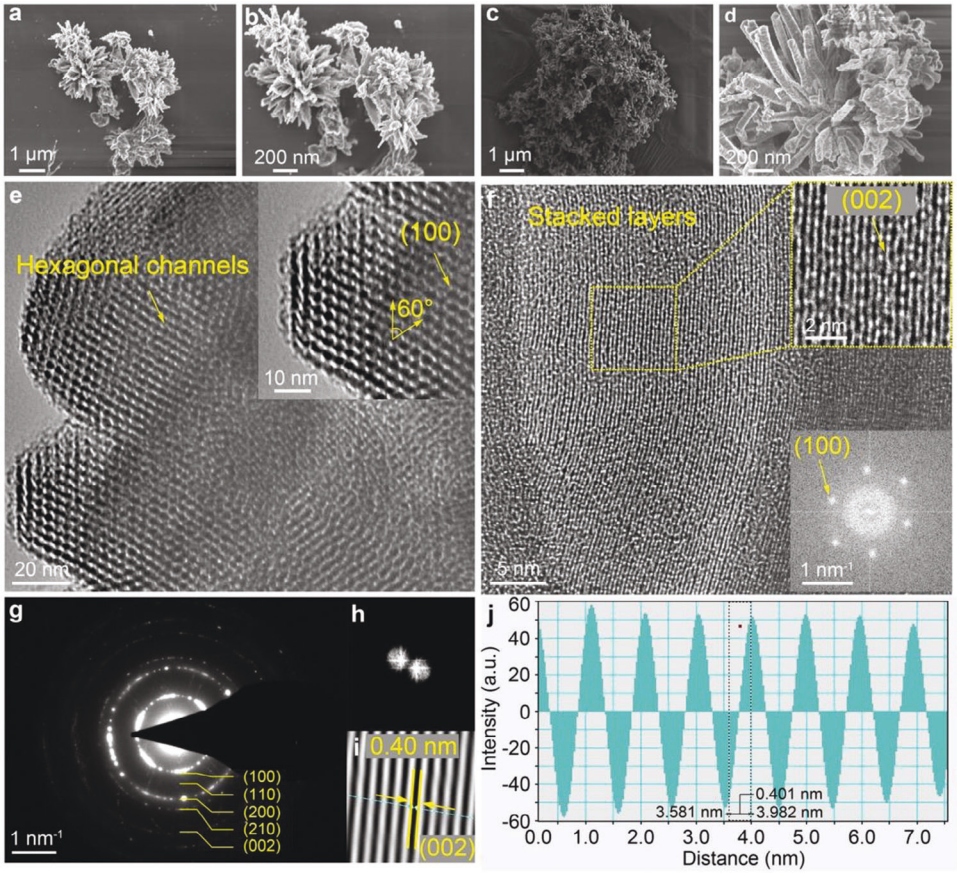

Figure 4. a,b) FE-SEM images of submicron flower-shaped TA-COF-1 particles. c,d) FE-SEM images of TA-COF-2. e) HRTEM image of TA-COF-1; (inset in e) arrows point to the (100) plane with hexagonal pore aperture, illustrating a 60° angle between two adjacent directions. f) Overview image of a TA-COF-1 particle, revealing continuous lattice fringes that span the entire particle from which higher-magnification image (top inset) was acquired at a region of interest (the marked yellow area), exhibiting (002) planes; (bottom inset in f) fast-Fourier transformation (FFT) filter applied on top inset of (f); the FFT of the area marked by the yellow box, cropped at the predominant fringe spacing, showing the hexagonal organization of pores featuring (100) phases. g) Selected area electron diffraction (SAED) pattern showing the presence of five distinct diffraction rings, (100), (110), (200), (210), and (002), corresponding to the crystal planes within the TA-COF-1 crystals. h) Mask applied on the FFT of TA-COF-1 layered area marked by the yellow box in (f) to select two central spots in the FFT. i) The HRTEM image in (f) after applying a Fourier filter to select the central spot along with two spots in the FFT. Magnification of the TA-COF-1 layered area showing the interlayer distance and the thickness of the layers and j) corresponding intensity profile plot of the designated line area in (i) after applying a bandpass filter. The intensity profile shows a constant and continuous periodicity, with a period of 0.40 nm.

In addition, a precisely organized frame border with a periodicity of 0.40 nm was observed (Figure 4f). This periodicity corresponded to the (002) plane, which was consistent with the *d* value of 0.37 nm at $2\theta = 25.3°$ in the PXRD pattern. We then measured the interlayer distance using DFT calculations and found that the theoretical value (0.37 nm) was in strong agreement with the assessed value from the microstructure (0.40 nm). The HRTEM images provided clear evidence of the long-range ordering of the TA-COF-2 structure, featuring a stacking distance of 0.41 nm (Figure S8, Supporting Information), aligning with the stacking distance calculated from the PXRD analysis in the simulated structure (Figure 1b).

To further confirm the high crystallinity, a fast-Fourier transformation (FFT) filter was applied to the layered area, indicating pronounced crystalline phases (Figure 4f, bottom inset; Figure S8d, Supporting Information). The FFT images revealed a pattern of white spots arranged in a hexagonal formation, which signifies the presence of pores organized in a hexagonal manner with (100) facets. We also performed selected area electron diffraction (SAED) on various particle groups to clarify the crystalline planes (Figure 4g; Figure S8c, Supporting Information). We observed five distinct diffraction rings, (100), (110), (200), (210), and (002), corresponding to the crystal planes within the TA-COF crystals. An intensity profile plot in the layered area facilitated precise measurements of interlayer distances and layer thickness (Figure 4j; Figure S8g, Supporting Information).

The TA-COFs do contain identifiable regions of crystallinity that align with the simulated structures. Notably, their crystallinity surpasses that of the majority of reported COFs and is on par with COFs that have recently been reported.[12,45–47] In addition to these regions of high crystallinity, the presence of less organized lattice configurations and defects in some regions is worth noting. This observation suggests the occurrence of defects within the crystalline lattice.[45]

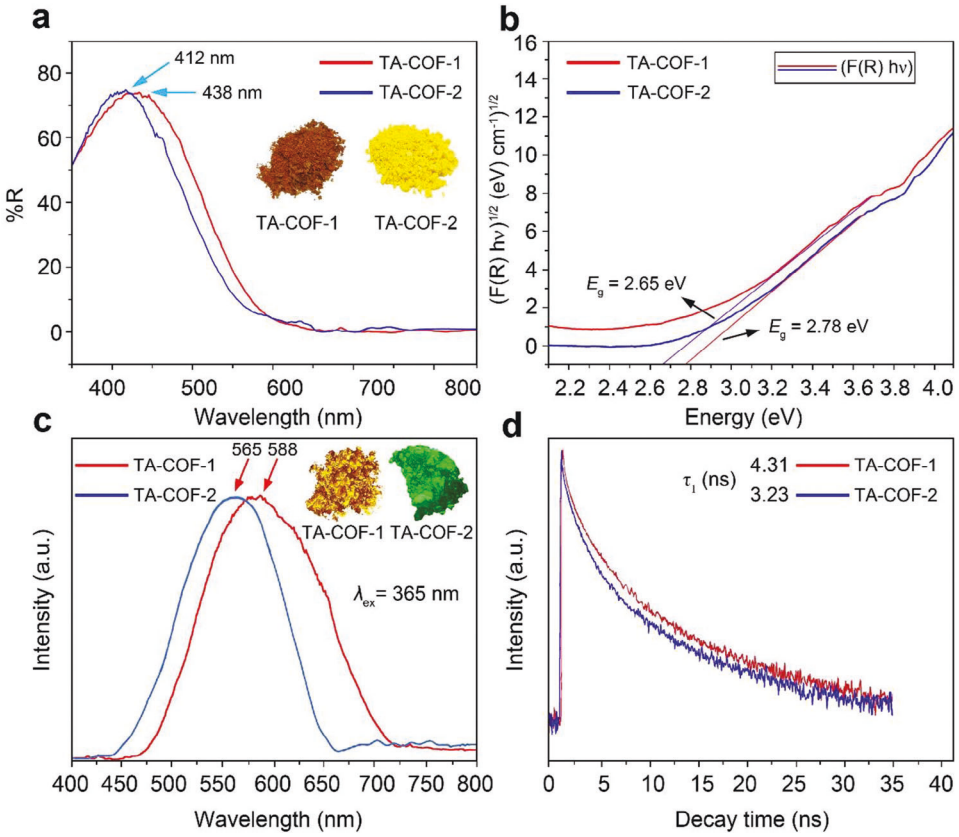

Figure 5. a) Solid-state UV–vis diffuse reflectance of TA-COF-1 (red) and TA-COF-2 (blue). Inset represents digital photographs of the TA-COFs under visible light. b) The optical bandgap of TA-COF-1 (red) and TA-COF-2 (blue) evaluated from the Kubelka–Munk function. c) The fluorescence spectra of TA-COFs upon excitation at 365 nm, TA-COF-1 (red), and TA-COF-2 (blue). Inset represents digital photographs of the same samples under UV lamp (365 nm). d) Fluorescence decay exponential time fit scan of TA-COF-1 (red broken line) and TA-COF-2 (blue broken line) under excitation at 365 nm.

The stratified arrangement in a large part of TA-COFs offers a convenient pathway for the photogenerated charge carriers to reach the surface, thereby facilitating photocatalytic reactions.

The thermal stability of the TA-COFs was studied by thermogravimetric analysis (TGA). The thermograms showed almost no mass was lost until 514 °C for TA-COF-1 and 521 °C for TA-COF-2, indicating that TA-COFs are stable up to 500 °C under nitrogen atmosphere (Figure S9, Supporting Information). The char yield (the remaining carbon after complete degradation of the substance at 800 °C under nitrogen atmosphere) was 62% for TA-COF-1 and 65% for TA-COF-2. We attribute the high char yield of TA-COFs to the decomposition of the tetrazine rings during heating. When these rings are decomposed, they reduce the distance between the three vinyl linked benzene rings and this proximity leads to significant char formation.[48] The combination of high decomposition temperatures and high char yields indicates that TA-COFs are quite thermally stable.

2.2. Photophysical Properties of TA-COFs

Solid-state ultraviolet–visible (UV–vis) diffuse reflectance and photoluminescence (PL) spectroscopies were used to probe the electronic transitions within the TA-COF during photocatalysis. The UV–vis showed maxima at 438 nm for TA-COF-1 and 412 nm for TA-COF-2, which were in line with their orange and yellow colors under visible light. Further, the broad peak from 400-600 nm indicates that TA-COFs could harvest photons in a wide area of the visible region (**Figure** 5a). The absorption edge value of TA-COF-1 (590 nm) was red-shifted ≈20 nm (570 nm) for TA-COF-2. We attribute this to the existence of more benzene knots and the associated increased rotation between the benzene rings in TA-COF-2, which leads to a greater weakening of π-electron delocalization within the framework. With weakened π-delocalization, the energy required for electronic transitions is reduced, leading to the absorption edge occurring at a shorter wavelength.[44] From the visible reflectance data and the Kubelka-Munk equation, the optical band gaps were (E_g) found to be 2.65 eV for TA-COF-1 and 2.78 eV for TA-COF-2 (Figure 5b).

Under irradiation at 365 nm, powders of TA-COF-1 emitted yellow luminescence and TA-COF-2 emitted green luminescence. Upon excitation at 365 nm, TA-COF-1 exhibited a maximum emission at 588 nm owing to its pronounced π-delocalization. In contrast, TA-COF-2 showed a slightly shorter maximum emission at 565 nm under the same conditions. This emphasizes the significance of π-electron delocalization in shaping the photophysical properties of these COFs. The relatively shorter maximum emission observed in TA-COF-2 can be attributed to the greater number of its benzene knots, resulting in a more pronounced reduction in π-electron spread throughout

the framework (Figure 5c). Both fluorescence decays show well-fitted exponential decay behavior (Figure 5d). From the PL decay curves, the average lifetimes of 4.31 and 3.23 ns are measured for TA-COF-1 and TA-COF-2, respectively. The narrow band gap of TA-COF-1 contributes to its longer fluorescence lifetime. This can be attributed to TA-COF-1's lower energy transition state which reduces the efficiency of non-radiative (fluorescence) relaxation processes. This lower energy transition state allows the excited state to persist for a longer duration, increasing the probability of radiative emission of photons. TA-COF-2; however, has a wider band gap which requires more energy for electronic transitions. This leads to shorter fluorescence lifetimes due to a more efficient non-radiative relaxation process involving the transformation of energy into heat.[49]

The influence of crystallinity on the photophysical properties of materials, especially polymers and COFs, is a critical factor that can impact their optical performance.[50] To uncover the impact of crystallinity on optical performance, a sample of TA-COF-1, that was used as a photocatalyst for the oxidation of 4-(trifluoromethylphenyl)boronic acid to 4-trifluoromethylphenol over 12 cycles of repetitive reactions, was selected for analysis. Comparisons between the crystallinity of this sample, called TA-COF-1-Low, and freshly made and unused TA-COF-1 were made based on the full width at half maximum of the distinct and sharp peak in the PXRD pattern corresponding to the (100) crystal plane. The value for TA-COF-1 was measured at 0.26°; while, that of TA-COF-1-Low exhibited a slight broadening with the peak measuring 0.40° (Figure S10, Supporting Information).

The fluorescence emission spectra of both TA-COF-1 and TA-COF-1-Low were measured to determine the impact of crystallinity. In the sample of TA-COF-1-Low, we observed a slight blue-shift from 586–572 nm (Figure S11, Supporting Information). This shift in emission wavelength was also reflected in the fluorescence decay patterns, with measured lifetime values of 4.31 ns for TA-COF-1 and 3.96 ns for TA-COF-1-Low (Figure S12, Supporting Information).

These findings provide evidence that the higher crystallinity of TA-COF-1 resulted in a lower charge carrier recombination rate and increased space charge separation. This effect is attributed to larger energy differences between the π and π^* levels, promoting longer-lived excited states in the material with higher crystallinity.[51] The organized, crystalline structure of COF layers creates well-defined electronic states, where the energy levels of electrons are distinct and quantized. This organization is crucial for the absorption and emission of light. Well-defined electronic states contribute to specific energy transitions, leading to characteristic absorption and emission spectra. This spectral specificity enhances the efficiency of light emission as electrons transition between these well-defined states with minimal energy loss.[52]

In highly crystalline COF structures, the ordered arrangement restricts the motion of molecules within the material. This limitation on molecular motion is significant because it reduces non-radiative processes which are pathways that do not involve the emission of light. Simultaneously, this ordered structure facilitates efficient charge separation, decreasing the likelihood of charge carriers recombining before emitting light.[53] By impeding non-radiative processes, crystalline regions promote radiative processes such as fluorescence, resulting in enhanced fluorescence efficiency. Moreover, the restricted molecular motion in highly crystalline regions contributes to longer lifetimes of excited states as the electrons experience fewer non-radiative decay pathways.[54] In regions with defects or lower crystallinity, there is increased molecular motion within the COF structure. This enhanced molecular motion promotes non-radiative decay pathways, where excited electrons dissipate energy without emitting light. As a consequence, the photoluminescence efficiency is reduced, and the excited states have shorter lifetimes due to the prevalence of non-radiative processes. The observed relationship between crystallinity and enhanced fluorescence efficiency aligns with existing literature that commonly report a correlation between crystallinity and increased charge separation and its impact on fluorescence spectra.[55–57] This correlation supports our findings and provides a theoretical foundation for the impact of crystallinity on charge dynamics and light emission. Overall, the degree of crystallinity in COFs is a key determinant of their photophysical properties, particularly in influencing light emission behavior.[58]

2.3. Chemical Stability

To evaluate chemical stability, the TA-COFs were treated in 6 M NaOH, 6 M HCl, trifluoroacetic acid (TFA) (concentrated, 13 M), Milli Q water, and under visible light for 7 days, and we performed a PXRD analysis to identify any changes (Figures S13 and S14, Supporting Information). Under these conditions, the crystallinity remained intact without any observed degradation, which is in contrast to many reported COFs.[59–61] Specifically, boronate ester-linked COFs exhibited weak hydrolytic stability;[60] while, imine-linked COFs underwent a backward reaction with reversible covalent bonds in acidic conditions.[62]

In addition, the TA-COFs were hydrophobic indicated by their contact angle, measured under the same experimental temperature and pressure conditions (Figures S15 and S16, Supporting Information). The contact angle values with water were measured as 62.9° ± 0.03° for TA-COF-1 and 68.4° ± 0.07° for TA-COF-2. We attribute the lower contact angle observed for TA-COF-1 to its higher porosity. Surfaces with larger pore volume and higher porosity have smaller contact angles because they tend to have greater surface area; and therefore, more interactions with water. This can result in increased wettability and decreased contact angles.[64]

During our investigation of the chemical stability of the TA-COFs, we observed a color change upon the addition of acid. This observation piqued our interest and led us to further study the acid sensitivity of TA-COFs; thus, we examined the influence of the electronic structure of the material under acidic conditions. A suspension of TA-COF in 1,4-dioxane (0.1 mg mL^{-1}) was prepared and the fluorescence, upon exposure to different concentration of HCl (0 to 59.6 µmol L^{-1}), was measured (**Figure 6a**; Figure S17, Supporting Information). Under excitation at 465 nm, the HCl-treated TA-COF-1 suspension exhibited a yellow fluorescence. There was a linear correlation between the fluorescent intensity and the HCl concentration in the suspended TA-COFs (0.5 mg mL^{-1}) in 1,4-dioxane. The addition of 10 µL of HCl (5.0 µmol L^{-1}) to the TA-COF-1 suspension resulted in the peak intensities at 507 and 525 nm diminishing while a new peak appeared at 556 nm (Figure 6a). As the concentration

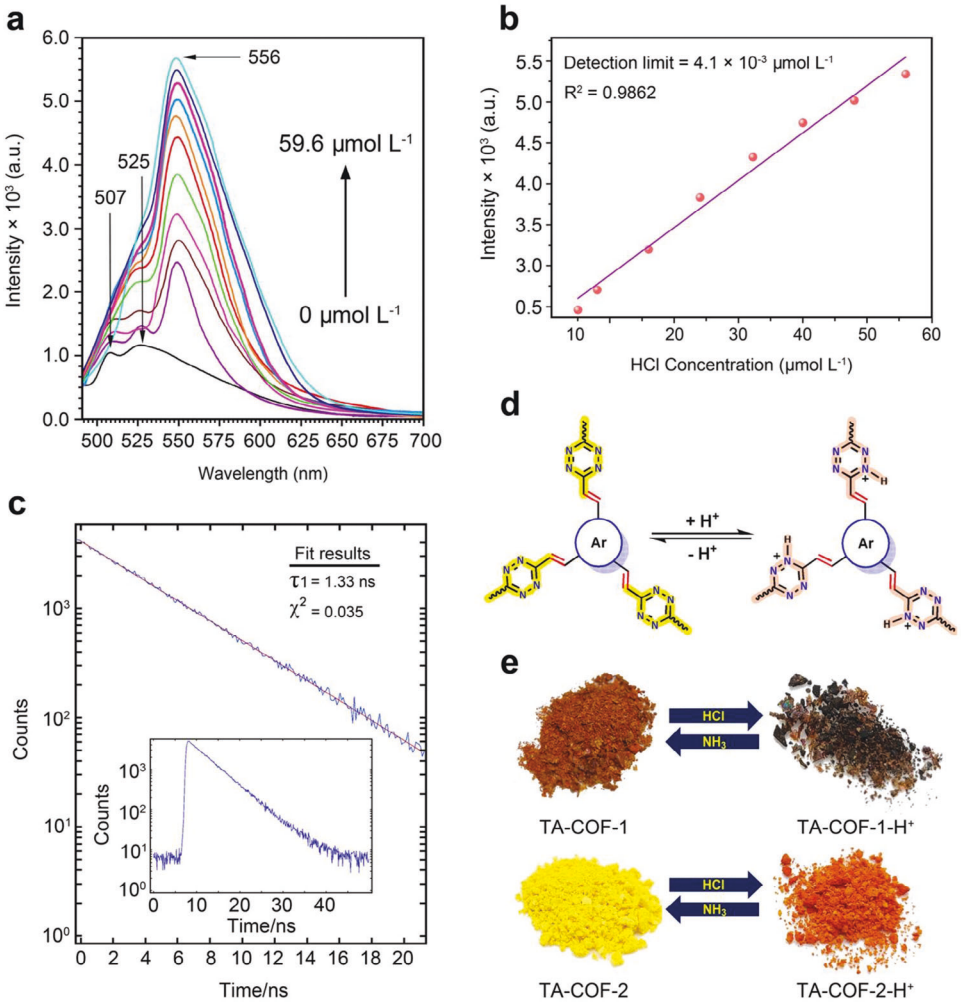

Figure 6. a) Fluorescence spectrum of acid-treated TA-COF-1 suspension (0.1 mg mL^{-1}) in 1,4-dioxane under excitation at 465 nm (acid concentration: 0–59.6 mmol L^{-1}). b) Correlation curve of fluorescence intensity versus acid concentration. c) PL decay spectra of TA-COF-1 monitored upon excitation at 365 nm. d) Possible protonation and deprotonation sites on TA-COF. e) Naked eye photographs of TA-COF powders upon exposure of HCl and NH_3 vapors.

of HCl increased from 6.0 to 59.6 μmol L^{-1}, the intensity of the peak at 556 nm steadily increased, and no noticeable change was observed at concentrations higher than 59.6 μmol L^{-1}. There was a linear relationship ($R^2 = 0.9862$) between the fluorescent intensity of the COFs and HCl concentration. Using calibration curve extrapolation, the lowest limit of detection was found to be 4.1 × 10^{-3} μmol L^{-1} (Figure 6b).

From the fluorescence decay curve, the lifetime of TA-COF-1 in HCl solution (59.6 μmol L^{-1}) was found to be 1.33 ns (Figure 6c). A plausible mechanism for HCl sensing suggested that under acidic conditions, the nitrogen heteroatom on each tetrazine ring was protonated. Protonation of tetrazine led to a substantial red-shift of the maximum for the π–π^* transition in the electronic absorption spectrum, from λ_{max} 295–336 nm. This was due to the substantial differences between the electronic structure of the base and its corresponding conjugate acid.[64] The substantial change in the electronic levels led to the observed color change (Figure 6d).[14] Such behavior has also been observed in few a previously reported COFs.[14–17]

The TA-COFs were also very sensitive to acidic and basic vapors. When TA-COF-1 and TA-COF-2 were exposed to HCl vapor, a reversible color change from orange to dark brown for TA-COF-1 and yellow to orange for TA-COF-2 was observed. Upon exposure to ammonia vapor, the COFs returned to their original colors (Figure 6e; Movies S1 and S2, Supporting Information). The response of our TA-COFs to HCl gas remained constant for several weeks. In extended experiments, no loss of acid-sensing capabilities despite repeated exposure cycles was observed. In addition, we performed PXRD analysis of COF samples after 30 acid-sensing cycles. The PXRD patterns showed that the crystal structure of TA-COF-1 and TA-COF-2 remained stable without significant damage or loss in crystallinity (Figures S18 and S19, Supporting Information). The diffraction peaks at different angles were consistent with the original COFs, confirming that their structural integrity was preserved.

The absorption spectra of the acid treated samples were studied by solid-state UV–vis diffuse reflectance spectroscopy and compared to the untreated TA-COFs. The maximum absorption

wavelength of TA-COF-2 (412 nm) red-shifted to 439 nm after acid treating and again blue-shifted to 425 nm after base treating (Figure S20, Supporting Information). The changes in absorption spectra observed after the acid and base treatment suggest that the chemical treatment altered the electronic structure of the material, which affected its light absorption properties; and thus, its color appearance.

Next, we theoretically studied the electronic structure and stability of TA-COFs and their protonated counterparts using the DFT method. The findings indicated distinct HOMO–LUMO gaps, measuring 2.51 eV for TA-COF-1 and 2.63 eV for TA-COF-2. However, the protonated forms of TA-COF-1 (TA-COF-1-H$^+$) and TA-COF-2 (TA-COF-2-H$^+$) exhibited a narrowing of the band gaps, measuring 2.03 and 2.28 eV, respectively, which was consistent with our experimental data. Upon protonation, noteworthy changes in torsion angles were observed. For example, in TA-COF-1, the torsion angle of C1–C2–C3–C4 shifted from 177.01° to 179.78°; while, the torsion angle of N1–C5–C6–C7 shifted from 168.16° to 179.90° (Figure S21, Supporting Information). Similarly, when it was protonated, the torsion angles in TA-COF-2 exhibited shifts from 177.81° to 179.94° for C1–C2–C3–C4 and 167.06° to 179.87° for N1–C5–C6–C7. These adjustments reflect an increase in the planarity of the TA-COF structures upon protonation. The expanded conjugation in the geometric configuration of protonated TA-COF-1 and TA-COF-2 explains the observed red-shift in absorption spectra and aligns with enhanced stability following the protonation.[65]

We then used time-dependent density functional theory (TD-DFT) calculations to predict and elucidate the electronic transitions governing the observed color changes. The TD-DFT calculations indicated three transition states, with one dominant transition characterized by the largest oscillator strength for both TA-COF-1 and TA-COF-2, as well as their respective protonated states. In the HOMO, electron distribution extends over the molecule along the molecular axis; while in the LUMO, electrons predominantly localize around the C=N bonds and benzene rings (Figure S22, Supporting Information). Notably, the lowest energy absorption for these compounds corresponded to the primary dipole-allowed π–π^* electronic transition from the HOMO to the LUMO. This absorption was attributed to intramolecular charge transfer, thereby offering a theoretical foundation for the observed color shifts in the context of the HCl and NH_3 interactions.[66]

Experimentally, we investigated the color change of our TA-COFs upon exposure to various acid vapors. We found that the color change was only observed in the presence of HCl vapor. Other acid vapors, such as HNO_3, HBr, trifluoroacetic acid (TFA), and acetic acid (AcOH) did not induce any noticeable change in the TA-COFs' color. This selectivity highlights the specific interaction between TA-COFs and HCl.

To better understand the sensitivity and selectivity of TA-COFs toward acidic solutions, we exposed the TA-COFs to 0.1 mmol L^{-1} concentrations of mineral acids and TFA and AcOH (Figures S23 and S24, Supporting Information). Only HCl triggered a substantial red-shift in the fluorescence emission maxima of the TA-COFs and resulted in remarkably strong fluorescence emission intensities, setting HCl apart from other acids in terms of sensitivity and responsiveness. We also observed slight variations in the maximum emission peak of TA-COFs as the acid type changed, organic versus mineral acids. Further, we introduced a 0.1 mmol L^{-1} NaCl solution into the other acidic solutions, which resulted in an additional increase in fluorescence intensity. This observation highlights the influence of counter ions in the system, potentially contributing to the slight variations in the maximum emission peak of TA-COFs when the acid type changes.[67,68] In conclusion, our results indicate that the TA-COFs exhibit selectivity toward HCl both in terms of vapor and acidic solutions.

2.4. Photocatalytic Oxidation of Arylboronic Acids to Phenols

The high chemical and photostability of TA-COFs makes them suitable for heterogeneous photocatalytic applications. TA-COFs were used as a photocatalyst in the oxidation of arylboronic acids to form the corresponding phenols (**Table 1**). Recently, catalytic oxidation of boronic acids to phenols was reported using COFs containing thiadiazole,[69] benzoxazole,[70] vinylene link,[71] and truxene[17] units, but the reactions required more than 48 h or resulted in lower yields.

Compared to earlier works, TA-COFs performed the catalytic oxidation reaction under milder conditions and much shorter reaction times, with high reusability and recyclability. We selected the hydroxylation of phenylboronic acid as a standard reaction to assess the photocatalytic performance of TA-COFs. This selection was made because tetrazine has a propensity to accept electrons and form radical anions, which can speed up the oxidation process.[72] Tetrazine possesses a high affinity for electrons, indicating that it can function as an electron-deficient component in a COF to reduce the energy level of its highest occupied molecular orbital (HOMO). Lowering the energy level of the HOMO can have important consequences for the COF's properties, such as its conductivity, reactivity, and stability.[73] The parameters that impact phenylboronic acid to phenol conversion, such as light (off or on), photocatalyst (with or without catalyst), and sacrificial agent, were systematically assessed.

A series of aryl phenols was quantitatively obtained using *N*,*N*-diisopropylethylamine (iPr_2NEt) as a sacrificial electron donor agent and TA-COFs as the photocatalysts under ambient atmosphere and blue LED light (Table 1). In the absence of the TA-COFs, no conversions were observed. Compared to the other COFs which were reported as photocatalysts for the oxidation of arylboronic acids, the TA-COFs illustrated higher activity.[17,69,70,74]

To evaluate the selectivity of the oxidation of arylboronic acids in the presence of diverse organic chemicals, we strategically selected arylboronic acids with reactive functional groups on their aromatic rings, including methyl, benzyl, aldehyde, and sulfur substituents (Table 1, entries 9–13). These functional groups represent a range of potential reaction partners that could influence the selectivity of the oxidation process. Under the conditions used, the arylboronic acids were successfully converted to their corresponding phenols in high yields, and the other functional groups remained intact. We did not observe any side reactions that could compromise the overall selectivity of the process.

To further underscore the selectivity of TA-COFs, we used them as photocatalysts for oxidizing arylboronic acids in the presence of *N*-phenyltetrahydroisoquinoline.

Table 1. Control experiments and substrate scope of TA-COFs in oxidation of arylboronic acids to phenols.

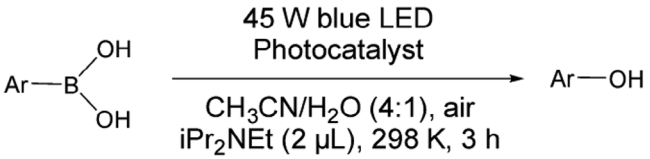

Entry[a)]	Ar	Light	Photocatalyst	Yield [%]	Ar—OH
1	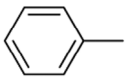	On	TA-COF-1 TA-COF-2 None	95 97 –	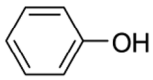
2	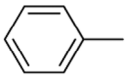	Off	TA-COF-1 TA-COF-2	– –	No reaction
3	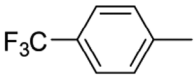	On	TA-COF-1 TA-COF-2	96 99	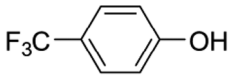
4	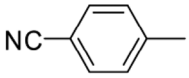	On	TA-COF-1 TA-COF-2	99 99	
5	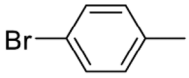	On	TA-COF-1 TA-COF-2	95 92	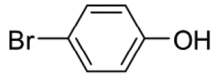
6	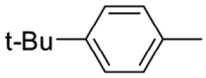	On	TA-COF-1 TA-COF-2	95 96	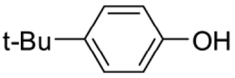
7	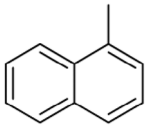	On	TA-COF-1 TA-COF-2	95 97	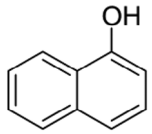
8	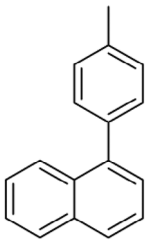	On	TA-COF-1 TA-COF-2	94 92	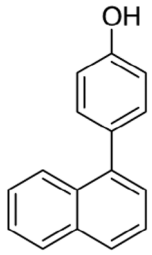
9	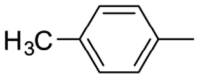	On	TA-COF-1 TA-COF-2	98 94	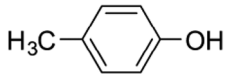
10	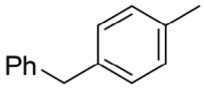	On	TA-COF-1 TA-COF-2	98 97	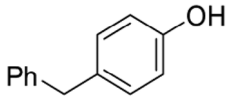
11	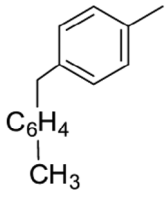	On	TA-COF-1 TA-COF-2	99 99	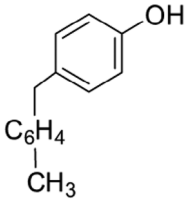

(*Continued*)

Table 1. (Continued).

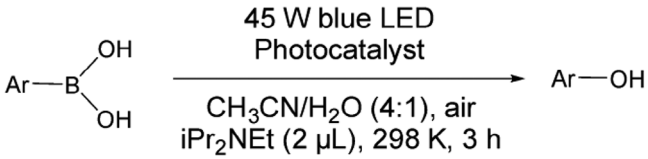

Entry[a)]	Ar	Light	Photocatalyst	Yield [%]	Ar—OH
12	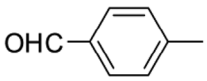	On	TA-COF-1 TA-COF-2	99 96	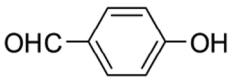
13	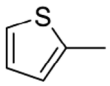	On	TA-COF-1 TA-COF-2	93 92	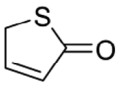

[a)] Conditions: TA-COF-1 (5.00 mg, 0.0103 mmol) or TA-COF-2 (7.50 mg, 0.0103 mmol), arylboronic acid (0.103 mmol), CH_3CN:H_2O (1.6 mL:0.4 mL), *N*,*N*-diisopropylethylamine (iPr_2NEt) (1.33 mg, 0.0103 mmol, 2 µL), irradiation of 45 W blue LED light at 298 K for 3 h. Ar = aryl group.

N-aryltetrahydroisoquinolines have the potential to form α-amino radicals under light irradiation and in the presence of photocatalysts such as metal–ligand complex catalysts.[75] The produced radicals can undergo dimerization reactions or react with nucleophiles to form radical addition products.[76] We did not observe any coupling reactions between the quinolines to form dimers, and the phenyl boronic acid was chemo-selectively converted to phenol at 95% yield. The *N*-phenyltetrahydroisoquinoline remained unchanged and unreacted in the mixture (Figures S25–S28, Supporting Information). The absence of side reactions and the successful conversion of arylboronic acids to phenols, even in the presence of various reactive functional groups or potentially interfering chemicals, reveals the robust and specific nature of the photocatalytic oxidation process catalyzed by TA-COFs.

The recyclability of TA-COFs was investigated using 4-(trifluoromethylphenyl)boronic acid as a model compound. The reaction was performed in excellent yield after 12 runs without any reactivation on the TA-COFs and no collapse was observed in the crystalline structures (Figure S29, Supporting Information). Our results of the catalytic reactions and the recyclability of the COFs were similar to those reported previously[69,77,78,111] and a plausible mechanism of arylboronic acid oxidation was developed (Figure S30, Supporting Information). The probable mechanism for this process was the formation of a superoxide radical ($O_2^{\bullet-}$). As mentioned before, the tetrazine linker was an active center. It had the potential to accept an electron to form a radical anion. Molecular oxygen would be converted to a superoxide radical which was detected by electron paramagnetic resonance (EPR). There was no signal when the DMPO solution was irradiated without TA-COFs (Figure S31, Supporting Information); however, in the presence of TA-COFs, the characteristic peaks associated with DMPO-$O_2^{\bullet-}$ were observed in a CH_3CN:H_2O (4:1 v/v) suspension under light irradiation.

We verified the existence of the $O_2^{\bullet-}$ intermediate using nitro-blue tetrazolium (NBT). The NBT underwent reduction by $O_2^{\bullet-}$, transitioning to its intense-blue diformazan configuration, thereby displaying its unique shade of purple (Figure S32, Supporting Information).[79] It is worth noting that $O_2^{\bullet-}$, in conjunction with a transferred electron, initiated an attack on ditetrazolium (NBT^{2+}), leading to the transformation of NBT^{2+} into a tetrazolinyl radical ($NBT^{\bullet+}$). This was succeeded by a subsequent electron transfer, converting $NBT^{\bullet+}$ into monoformazan. An overabundance of NBT or $O_2^{\bullet-}$ theoretically holds the potential to yield solely mono or diformazan products.[80] Therefore, we concluded that the oxidation of arylboronic acids is caused by the formation of $O_2^{\bullet-}$ on TA-COFs under light irradiation.

Based on our study, we propose that the mechanism that directs this oxidation process begins with an initial electron-transfer event which is catalyzed by the synergistic interaction between the boronic acid and a tertiary amine Lewis base (Figure S30, Supporting Information). It appears to rely upon the formation of a Lewis acid–base adduct that assumes the role of an electron acceptor. In electron deficient arylboronic acids with electron-withdrawing groups, the vacant p-orbital of the boron atom is more accessible to $O_2^{\bullet-}$.[81] When TA-COF is irradiated under blue LED light, the electron is excited from the valence band (VB) to the conduction band (CB), leaving a hole in the VB of TA-COF, and an exciton is generated. The excited electron can be quenched by O_2, making $O_2^{\bullet-}$. In the presence of $O_2^{\bullet-}$, the Lewis acid–base adduct undergoes a transformative collapse, leading to the generation of a boronic acid-superoxide radical anion adduct. This conversion is accompanied by the release of the base (iPr_2EtN). The detailed steps of how the electron moves during this single electron transfer (SET) need more careful study though it is similar to another report where pairs of chemicals come together and exchange electrons when exposed to light.[82] Van der Eycken and Ley[83] have shown this before, linking it to the established pathways along which light triggers chemical changes. Subsequent to the SET process, another electron transfers from the iPr_2NEt to the valence band of TA-COF and initiates the neutralization of the TA-COF, reverting it to its ground state. This transformation simultaneously produces a tertiary ammonium radical cation ($iPr_2NEt^{\bullet+}$), a key intermediate in the following steps. The boron superoxide radical anion intermediate then converts to boron hydroperoxide by hydrogen abstraction from an $iPr_2NEt^{\bullet+}$. Finally, the phenol is produced by the

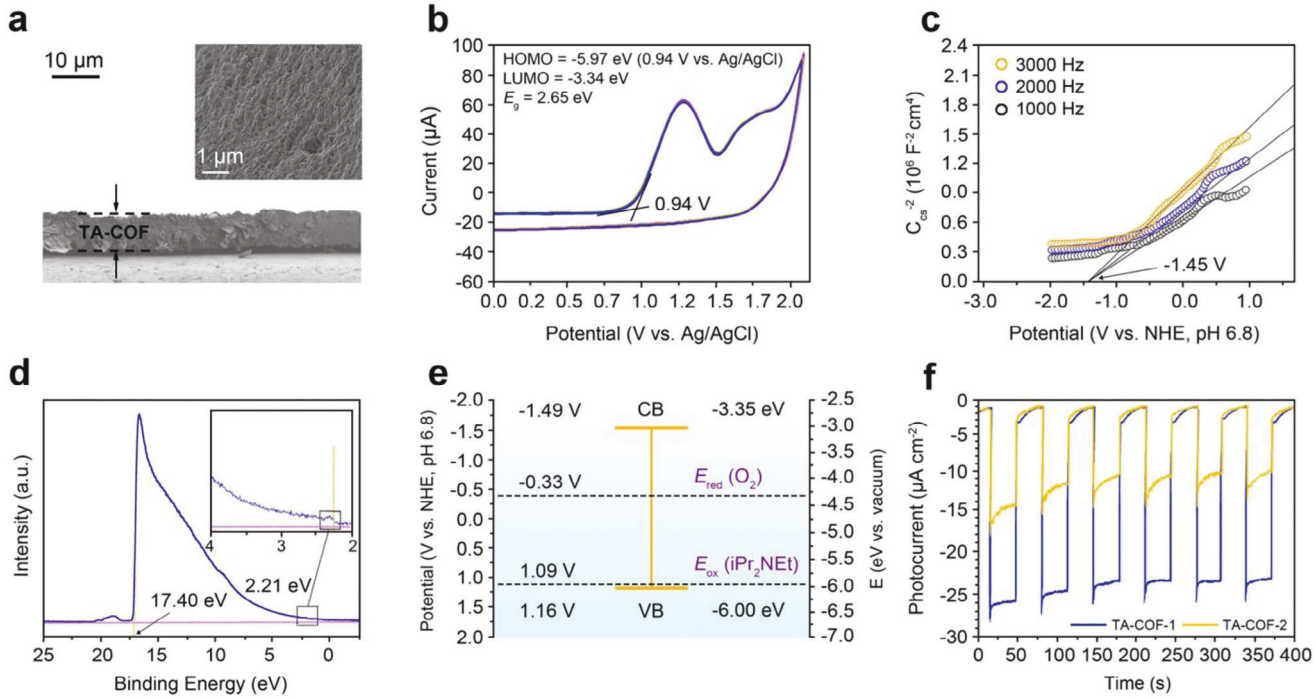

Figure 7. a) Cross-sectional and top view (inset) FE-SEM images of drop casted TA-COF-1 film showing the porous texture of the uniform film from both sides. b) CV curves of TA-COF-1 versus Ag/AgCl (+ 0.199 V) measured in a 0.2 M aqueous solution of Na_2SO_4 (pH 6.8). c) Mott–Schottky plots of TA-COF-1 film measured in 0.2 M Na_2SO_4 (pH 6.8) with Ag/AgCl (+ 0.199 V vs NHE) as the reference electrode in dark at 1, 2, and 3 kHz. d) UPS spectrum of TA-COF-1. e) Energy diagram for TA-COF-1, E_{red} of O_2, and E_{ox} of iPr_2NEt. f) Chopped cathodic photocurrent density versus time recorded on TA-COF films at 0.8 V versus NHE.

rearrangement of boron hydroperoxide anion into boron hydroperoxide, followed by hydrolysis.

2.5. Electrochemical Properties

Electrochemical methods were used to investigate the diverse electronic characteristics of TA-COFs. At first, the ability to form a film was evaluated by drop-casting suspensions of the TA-COFs in ethanol onto an indium tin oxide (ITO) surface without the addition of any other substances. The FE-SEM images captured from both a top–down and side angle perspective distinctly demonstrated the uniform porous texture of the resulting film, which measured several micrometers in thickness (**Figure 7**a; Figure S33, Supporting Information). The formation of a uniform film allowed us to study the semiconducting properties of TA-COFs using electrochemical methods.

The highest occupied molecular orbital (HOMO) and lowest unoccupied molecular orbital (LUMO) levels were determined using cyclic voltammetry (CV). The CV curves of TA-COF-1 and TA-COF-2 in a 0.2 M aqueous solution of Na_2SO_4 (pH 6.8) showed a reversible oxidative and reductive process during multiple scans, indicating good electrochemical stability (Figure 7b; Figure S34, Supporting Information). The HOMO and LUMO levels were determined by measuring the average oxidation potentials of TA-COF-1 and TA-COF-2 versus Ag/AgCl (saturated KCl) and were found to be 0.94 and 1.12 V, respectively. These values corresponded to a HOMO level of −5.97 eV and a LUMO level of −3.34 eV for TA-COF-1, and a HOMO level of −6.16 eV and a LUMO level of −3.38 eV for TA-COF-2.

More accurate HOMO/LUMO energy level values were determined by other electrochemical techniques. The type of conductivity, flat band potential (E_{fb}), and relative band positions of the TA-COFs were determined by Mott–Schottky analysis in an aqueous solution of 0.2 M Na_2SO_4 at pH 6.8.[84] The positive curve of the slope indicates a typical behavior of n-type semiconductors and is present for both TA-COFs, where electrons are the primary carriers (Figure 7c; Figure S35, Supporting Information).[85] This discovery is consistent with the COF construction, which has high π-electron conjugation between the vinyl-tetrazine linkers.[86] By examining the linear region of the Mott–Schottky plots, the E_{fb} at pH 6.8 was found to be −1.45 V for TA-COF-1 and −1.61 V for TA-COF-2 versus normal hydrogen electrode (NHE). According to the Mott–Schottky equation, the slope of the plot of the capacitance (C) versus the applied potential depends on the effective density of states in the VB and CB. The E_{fb} of a semiconductor can be more negative than that of another material if it has a higher effective density of states in the VB or a lower effective density of states in the CB, leading to a steeper slope (a more negative slope) in the Mott–Schottky plot.[87] If we consider two semiconductors with at least a small difference in structure, the slope of their Mott-Schottky plots will be different. Specifically, if the semiconductor with the larger effective density of states in the VB has a steeper slope than the other semiconductor, then it will have a more negative E_{fb}.[88] This occurs because the slope of the Mott–Schottky plot is related to the concentration of charges near the

semiconductor surface. A steeper slope indicates a higher concentration of charges, which in turn results in a more negative E_{fb}.[89] TA-COF-2 had a more negative E_{fb} than TA-COF-1, indicating that the stronger electron-donating tris(biphenylene)benzene units present in TA-COF-2 may have decreased the conduction band minimum (CBM): the LUMO energy. The CBM potential of n-type semiconductors is typically slightly negative, usually ≈0.1–0.2 eV lower than their E_{fb}.[90] Therefore, it is expected that semiconducting TA-COFs will have CBM potentials that are much more negative than their oxygen reduction potential (E_{red}) (−0.33 V vs NHE), which theoretically creates a strong driving force for the reduction of oxygen to superoxide radical.[91]

To measure the valence band maximum (VBM), the HOMO levels, in the solid state, ultraviolet photoelectron spectroscopy (UPS) was used. To calculate the VBM values, the excitation energy (21.22 eV) was subtracted from the width of the He (I) UPS spectra. By measuring the VBM levels of TA-COF-1 (Figure 7d) and TA-COF-2 (Figure S36, Supporting Information), the VBM levels were found to be −6.00 and −6.27 eV versus vacuum level, respectively. It was possible to determine the CBM of TA-COF-1 by using the optical band gap. This value was calculated to be −3.35 eV versus vacuum level (equivalent to −1.49 V vs NHE at pH 6.8), and it was found to be relatively similar to the E_{fb}. The corresponding value for TA-COF-2 was calculated to be −3.49 eV versus vacuum level (−1.35 V vs NHE at pH 6.8). The energy band diagrams of TA-COF-1 and TA-COF-2 indicated that the energy levels of the three components were in line such that the CBM was much more negative than the E_{red} of O_2 for the reduction of O_2 to superoxide radical (Figure 7e; Figure S37, Supporting Information).

To compare the CBM and VBM energy levels of TA-COFs, the E_{red} of O_2 and the oxidation potential (E_{ox}) of iPr_2NEt versus NHE were found to be −0.67 and +1.09 V.[92] For a photocatalyst to facilitate the reduction of O_2 and the oxidation of iPr_2NEt, its CBM value should be lower than that of E_{red} of O_2 and its VBM value should be higher than that of E_{ox} of iPr_2NEt. For both TA-COFs, the measured values of E_{red} were lower than O_2, and the measured values of E_{ox} were higher than those of iPr_2NEt.

To assess the photoelectric properties of these COFs, photocurrent tests were conducted using their film electrodes on ITO substrates submerged in a 0.2 M Na_2SO_4 solution at pH 6.8. Both TA-COFs generated transient photocurrent with different responses upon irradiation with visible light (>400 nm) using a Xe lamp. The chopped current–potential curves of the TA-COFs photoelectrodes showcased an impressive photo-response when subjected to light on/off switching (Figure 7f). When a bias potential of 0.8 V versus reversible hydrogen electrode (RHE) was applied, a cathodic photocurrent was detected with a saturated current density of ≈27 μA cm^{-2} for TA-COF-1, which was higher than that of TA-COF-2 (15 μA cm^{-2}). TA-COF-1 exhibited the highest photocurrent response indicating a more rapid internal charge transfer.[93]

In comparison to organic photocathode VCOFs and various other COF types reported in the literature, and most recently reported carbon nitrides (Table S2, Supporting Information), the TA-COFs rank highest in terms of photocurrent response and photoconductivity. Upon interruption of the irradiation, the photocurrent rapidly decreased to the steady-state value (nearly zero), and the original value of the photocurrent was reverted once the light was switched on again. During a series of repeated on/off illumination cycles (30 s light on, then 30 s light off per cycle) at 0.8 V in 400 s measurement period, the photocurrent density of the TA-COFs remained relatively constant, suggesting exceptional stability when exposed to light irradiation. The remarkable photophysical and chemical properties and electrochemical behaviors of the TA-COFs motivated further investigation into their potential applications in photocatalytic oxidative imine coupling reactions.

2.6. Photocatalytic Oxidation of Benzylamine Derivatives

The TA-COFs were also explored as metal-free heterogeneous photocatalysts for the oxidation of benzylamine derivatives to their corresponding *N*-benzylidenebenzylamines under blue LED light (**Table 2**). Primary benzylamines, regardless of any electron donating groups such as methyl and methoxy, or electron withdrawing groups such as chloro, fluoro, or trifluoromethyl groups, were converted to the related imines in greater than 91% yields, indicating that the substrate's electronic environment had no impact on the performance of the catalyst. Moreover, the stability of TA-COF-1 was also investigated after the oxidation process and the PXRD patterns of TA-COF-1 did not change appreciably (Figure S38, Supporting Information). This high catalytic activity could be due to the existence of very active tetrazine linkers and the high porosity of TA-COFs.

A mechanistic pathway for the light-assisted oxidative coupling of benzylamines begins with the amine adsorbing onto the surface of the TA-COF (Figure S39, Supporting Information).[94] Under the influence of light, the TA-COF is photoexcited to generate electron and holes. In the meantime, the electrons move from the adsorbed benzylamine to the TA-COF through a charge transfer process. Electrons collected in the CB of the TA-COF reduce molecular oxygen (O_2) to $O_2^{\bullet-}$. An electron transfer then occurs from benzylamine to the hole of the TA-COF, resulting in the formation of a benzylamine intermediate. Subsequently, the α-hydrogen of the benzylamine radical cation transfers to the TA-COF.[95] In the presence of $O_2^{\bullet-}$, the transferred hydrogen atom to the TA-COF produces H_2O_2 and the amine is converted to C_6H_5—CH=NH as an intermediate. During the reaction of benzylamine and C_6H_5—CH=NH intermediate in the presence of H_2O_2, benzaldimine and ammonia are formed.[96]

2.7. Sunlight-Driven Catalytic Photolysis of 5-Nitro-1,2,4-1riazol-3-one (NTO)

To capitalize on protonated TA-COFs potential to act as both a photocatalyst and a Brønsted acid, we explored their use toward the catalytic photolysis of the insensitive munition 5-nitro-1,2,4-1riazol-3-one (NTO). Insensitive munitions are less reactive to accidental explosions from fires, bullets, or other shrapnel leading to increased munitions safety,[97] replacing conventional explosives, such as TNT, due to concerns about accidents, toxicity, and mutagenicity.[98] IMX-101 is a complex insensitive explosive compound featuring NTO, nitroguanidine (NQ), and 2,4-dinitroanisole (DNAN), which stands out for its stability and energy performance, yet its use generates substantial wastewater

Table 2. Light-induced photocatalytic oxidative coupling of substituted benzylamines over TA-COFs.

Entry[a]	Substrate	Light	Photocatalyst	Yield [%][b]	Product
1	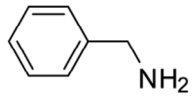	On	TA-COF-1 TA-COF-2 None	97 97 –	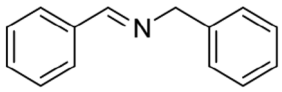
2	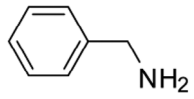	Off	TA-COF-1	–	No reaction
3	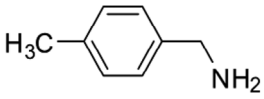	On	TA-COF-1 TA-COF-2	99 97	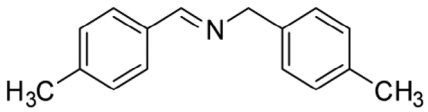
4	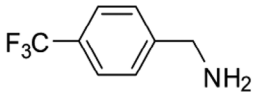	On	TA-COF-1 TA-COF-2	99 99	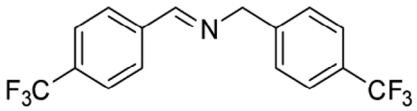
5	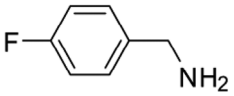	On	TA-COF-1 TA-COF-2	95 95	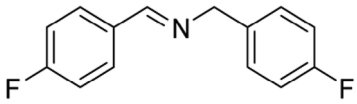
6	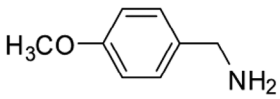	On	TA-COF-1 TA-COF-2	90 91	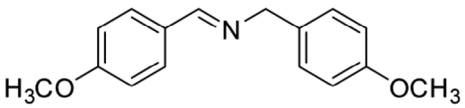

[a] Conditions: TA-COF-1 (5.00 mg, 0.0103 mmol) or TA-COF-2 (7.50 mg, 0.0103 mmol), arylamine (0.103 mmol), CH_3CN (1 mL), under a 1 atm O_2 atmosphere, irradiation by a blue LED light at 298 K for 2 h; [b] Determined by ^1H NMR of the crude mixture.

that contains unreacted NTO which requires simple and fast remediation methods.[99]

Despite NTO's stability, its notable solubility in water presents environmental concerns.[100] Prior research in this area explored microbial degradation under diverse conditions, yet complete degradation remains hindered by NTO concentrations.[101] In response, NTO photo-oxidation has emerged as a promising environmentally sustainable approach.[100] Despite this, research on catalytic NTO photolysis has been somewhat limited, primarily using two oxidation methods: titanium oxide (TiO_2) or hydrogen peroxide.[102,103] Of these, UV photolysis combined with hydrogen peroxide has shown promising results, primarily attributed to the generation of hydroxyl radicals that enhance the oxidation of organic compounds. Unfortunately, the absorption of hydrogen peroxide in the near UV region is limited and showed only low reaction efficiency for more than 10 h toward the catalytic photodegradation of NTO.[100,112] Moreover, it was observed that the addition of hydrogen peroxide to the TiO_2 suspension led to a reduction in the reaction rate. This effect could be attributed to the reaction of hydrogen peroxide with hydroxyl radicals which resulted in a decrease in the concentration of hydroxyl radicals within the reaction medium.[102]

While hydrogen peroxide did not efficiently degrade NTO, it was found that NTO degradation could be facilitated in acidic environments.[104] As tetrazine is a weak base, its conjugated acid functions as a strong Brønsted acid,[105] and protonated TA-COFs possess a narrowed band gap post-protonation; thus, protonated TA-COFs can serve both as photocatalysts and Brønsted acids. These distinctive attributes led us to investigate TA-COFs for the catalytic photolysis of NTO.

We investigated both protonated and unprotonated TA-COFs with respect to NTO photolysis efficacy. As expected, the photolysis reactions were accelerated in the presence of protonated TA-COFs, and NTO was completely degraded within 20 min while TiO_2 required at least 180 min. The reaction was conducted under sunlight conditions without using a UV source or a photosensitizer for the photolysis unlike the TiO_2 experiments which did employ short UV radiation ($\lambda < 190$ nm).

We evaluated the impact of protonated and unprotonated TA-COFs on sunlight-driven photolysis efficiency by examining how NTO fragmentation time was affected (**Figure 8**). In the absence

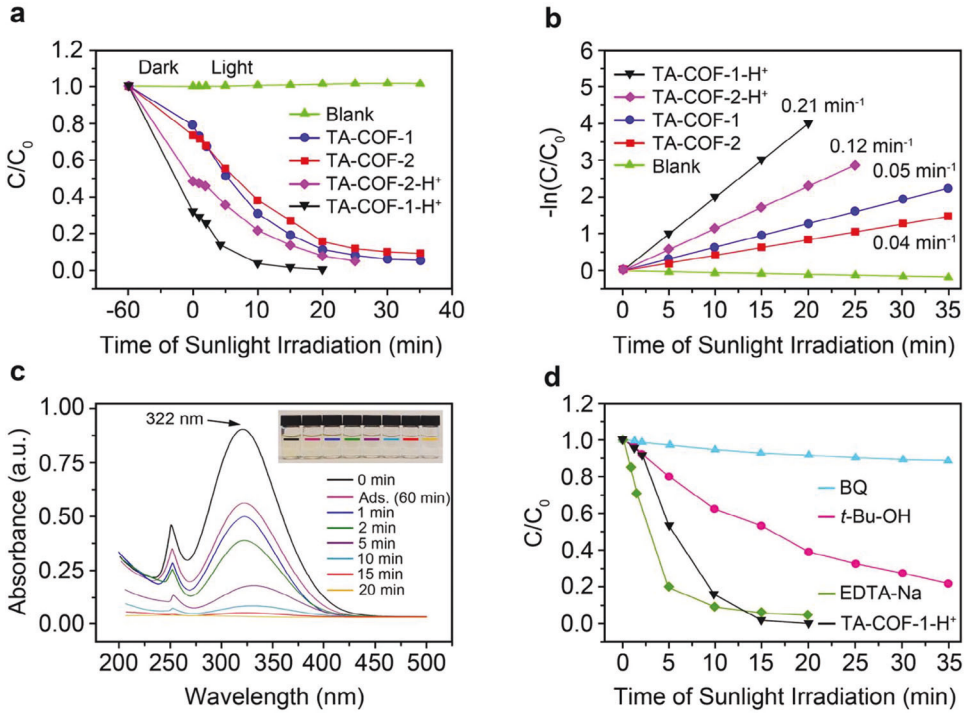

Figure 8. a) Sunlight-driven photocatalytic degradation of NTO (150 mg L^{-1}) using protonated and unprotonated TA-COF photocatalysts. b) Kinetics of NTA photodegradation with linear simulatin curves and apparent reaction rate constants (k) for different photocatalyts. c) Evolution of UV–vis absorption spectra of NTO with irradiation time using TA-COF-1-H^+. d) Photodegradation of NTO over TA-COF-1-H^+ in the presence of various scavengers, with C_0 as the initial NTO concentration following dark adsorption tests.

of any photocatalyst, decomposition of NTO didn't occur under sunlight exposure. First, to achieve an equilibrium state for adsorption and desorption between NTO and TA-COF, the mixture was gently agitated in darkness for 1 h before being exposed to visible light.

TA-COF-1-H^+ and TA-COF-2-H^+ exhibited enhanced capabilities for the photodegradation of NTO compared to their unprotonated counterparts. A rapid decrease in the concentration of NTO was observed, occurring within 20 min of exposure to sunlight in the presence of TA-COF-1-H^+ and 25 min for TA-COF-2-H^+ (Figure 8a). Unprotonated TA-COFs displayed slightly lower photocatalytic activity compared to the protonated TA-COFs (Figure 8b). We attribute the dual nature of the protonated TA-COFs to the improvement in the transfer of photogenerated electrons within the heterojunction and the creation of an acidic reaction medium, which collectively facilitated the degradation of NTO.[105]

To confirm the acidic nature of the tetrazine linker, we measured the zeta (ζ) potentials of the protonated and unprotonated TA-COF-1 and TA-COF-2 at varying solution pH levels (Figure S40, Supporting Information). The point of zero ζ potential, indicating the transition from positive to negative surface charges, occurred at pH 2.93 for TA-COF-1, pH 3.37 for TA-COF-2, pH 8.41 for TA-COF-1-H^+, and pH 8.72 and for TA-COF-2-H^+. This shift in ζ potential serves as a clear indication of the protonation of the tetrazine linker in both TA-COF-1-H^+ and TA-COF-2-H^+, making each COF acidic under specific pH conditions. Specifically, at pH levels below 8, the ζ potentials of TA-COF-1-H^+ solutions were positive and remained relatively constant over the range of pH 8–3, with only minor increases; then, they increased dramatically when decreasing solution pH values dropped below pH 3. Conversely, above pH 8, the positive ζ potentials decayed rapidly, becoming negative at pH levels above 8.41, reaching a substantial value of ≈ −28.2 mV at pH 12.

Similar trends were observed for TA-COF-2. The point of zero zeta potential for TA-COF-2-H^+ was found at pH 8.72, confirming the protonation of the tetrazine linker. This is consistent with the behavior observed for TA-COF-1-H^+, indicating that the protonation and deprotonation processes in TA-COF-2-H^+ exhibit dynamic characteristics, aligning with the changes seen in TA-COF-1-H^+.

The distinct difference in ζ potentials between the protonated and unprotonated forms of TA-COFs further supports the conclusion that the protonation of the tetrazine linker imparts an acidic character to the TA-COFs. This acidity, along with the reduced energy band gaps observed in protonated TA-COFs, underscores their distinctive dual functionality as both a photocatalyst and a Brønsted acid catalyst, promoting efficient photocatalytic degradation of NTO.

The impact of varying catalyst loading on the photolysis efficiency of NTO was investigated by introducing different quantities of TA-COF samples, ranging from 1–5 mg, into 10 mL of a 150 mg L^{-1} NTO solution under sunlight at room temperature for a duration of 20 min. As the amount increased from 1–3 mg, the photodegradation efficiency of NTO improved from 47.0% to 99.9%. Concentrations above 3 mg had no discernible impact on the efficiency.

The photodegradation kinetics follow a pseudo-first-order reaction model ($-\ln(C/C_0) = kt$), where k represents the apparent rate constant.[106] Protonated TA-COFs displayed a distinct increase in photocatalytic capacity compared to their parent TA-COFs (Figure 8c). The photodegradation efficiency of TA-COF-1-H^+ was the highest, with an apparent rate constant of 0.21 min^{-1}. This rate was four times greater than that of original TA-COF-1 (0.05 min^{-1}) and more than five times higher than that of TA-COF-2 (0.04 min^{-1}).

Subsequently, an examination of the recyclability and stability of TA-COF-1-H^+ was conducted and proved to have high photocatalytic efficiency exceeding 92% over 12 cycles (Figure S41, Supporting Information), and the chemical structure and morphology of TA-COF-1-H^+ remained unchanged as evidenced by PXRD and FT-IR analyses (Figures S42 and S43, Supporting Information). To the best of our knowledge, this marks the first known instance of a COF being used for the sunlight-driven catalytic photolysis of NTO.

To explore the photocatalytic mechanism of TA-COF-1-H^+, radical trapping experiments were conducted to investigate the roles of active species in this process. Sacrificial agents, including *p*-benzoquinone (BQ), tert-butanol (*t*-Bu-OH), and ethylenediaminetetraacetic acid disodium salt (EDTA-2Na), were introduced as scavengers for superoxide radicals, hydroxyl radicals, and holes of the photoexcited catalyst, respectively. A significant reduction in NTO decomposition in the presence of BQ or *t*-Bu-OH confirmed the critical involvement of $O_2^{\bullet-}$ and $^{\bullet}OH$ in the degradation process (Figure 8d). In contrast, the rate of reaction accelerated with the addition of EDTA-2Na, which could be attributed to the competitive reaction of excess holes with EDTA-2Na, reducing the recombination rate and providing more available excess electrons for oxidative radical-mediated degradation.[107]

In light of these results, we propose a mechanism for the degradation of NTO by oxygen radical species (Scheme S1, Supporting Information). Under acidic conditions in a sequence of reactions, active radical species are generated in different ways (Scheme S1, Supporting Information, path a). In the first mechanism within the valence band of the photocatalyst, water undergoes photo-oxidation, resulting in the formation of hydroxyl radicals (Scheme S1, Supporting Information, path a, I). Conversely, in a complementary pathway, oxygen undergoes conversion into superoxide radicals through photo-reduction within the conduction band of the photoexcited catalyst (Scheme S1, Supporting Information, path a, II). These superoxide radicals can directly break down NTO.

Alternatively, in the presence of an acidic species, superoxide radicals can undergo a transformation into hydroperoxyl radicals ($HOO^{\bullet}$), the conjugate acid of superoxide, which has lower reactivity than hydroxyl radicals (Scheme S1, Supporting Information, path a, III). Within an acidic solution, the reduction of hydroperoxyl radicals is initiated, giving rise to the generation of hydroxyl radicals and hydroxyl ions (Scheme S1, Supporting Information, path a, IV). The hydroxyl ions undergo oxidation within the valence band of the photocatalyst, leading to the production of corresponding radicals (Scheme S1, Supporting Information, path a, V).[108] The oxidation catalyzed by hydroxyl radicals results in the transformation of NTO into triazol-dione (TAD) and substituted triazolones intermediates, and consequently, carbon dioxide, nitrates, and potentially ammonia (Scheme S1, Supporting Information, path b).[102]

The modeled pathways for NTO decomposition in water induced by superoxide radical with the selected molecular structures of the transition states initiate with the interaction of a superoxide radical and NTO (Scheme S1, Supporting Information, path c);[104] thus, initiating the addition of the radical to the carbon atom adjacent to the nitro group within the C=N double bond. This addition is succeeded by a nucleophilic addition to the carbonyl group, followed by intramolecular rearrangement and elimination of nitro acid to form dioxazole-3-one intermediate (DIO). The acid-catalyzed decomposition of DIO ultimately results in the generation of isocyanic acid, carbon dioxide, and nitrogen gas. Subsequently, isocyanic acid undergoes hydrolysis to form carbon dioxide and ammonia.

The above results highlight the key role of protonation in fine-tuning the characteristics of TA-COFs to improve their suitability for photocatalytic applications. Protonated TA-COFs represent a highly promising class of photocatalysts, known for their efficiency and flexibility in diverse environmental remediation and energy conversion processes; thus, presenting an environmentally sustainable solution to confront urgent global challenges. Subsequent investigations in this domain hold the potential to disclose further avenues for the utilization of these materials in cutting-edge catalytic applications.

3. Conclusion

In conclusion, we have synthesized two vinyl tetrazine-linked COFs using a well-established synthetic strategy. The synthesized COFs exhibited exceptional crystallinity, high surface areas, and well-defined π-conjugated frameworks. These COFs showed high photoactivity and a reasonably small HOMO-LUMO gap. Importantly, the synthesized COFs have also exhibited remarkable chemical stability, showcasing their robustness under rigorous conditions. They displayed exceptional resistance to strong acid (HCl 6 M), corrosive base (NaOH 6 M), and prolonged exposure to light for 7 days. This combination of high photoactivity and chemical stability positioned these COFs as promising candidates for a wide range of applications that demand both efficient catalysis and resistance to challenging environments.

As photocatalysts, the TA-COFs provided a metal-free option to light-assisted oxidation reactions, such as hydroxylation of arylboronic acids to the corresponding phenols and the oxidative coupling of substituted benzylamines to *N*-benzylidenebenzylamines. During photocatalysis, the reaction conversions were all higher than 90%, and the COFs retained crystallinity as monitored by PXRD. Significantly, they were easily recycled and showed only small changes in crystallinity after twelve catalytic cycles.

The obtained COFs exhibited the highest photocurrent response and photoconductivity among the evaluated materials. These results underscore the remarkable potential of TA-COFs as efficient photocathodes for a variety of applications. The superior performance can be attributed to the unique structural and electronic properties of TA-COFs, including high crystallinity, large surface area, and optimized π-conjugated frameworks.

TA-COFs are sensitive to hydrochloric acid, evidenced by significant changes in fluorescence intensity and emission

wavelength in response to varying HCl concentrations. Our investigation into TA-COFs' response to diverse acid vapors highlights their selectivity as they exclusively undergo a reversible color change upon exposure to HCl vapor, distinguishing it from other acids tested. TA-COFs displayed a reversible visible color change when subjected to both acidic and basic conditions, rendering them effective acid sensors toward HCl. Their rapid "turn-on" fluorescence response, observable by the naked eye, occurred in less than a second.

We have also shown that TA-COFs can effectively degrade NTO in sunlight conditions quickly by leveraging the dual nature of the protonated TA-COFs as a photocatalyst and a Brønsted acid. To the best of our knowledge, this represents the first instance of a COF being used for the photocatalytic degradation of NTO. A detailed comparison between protonated and unprotonated TA-COFs highlights the subtle influence of TA-COF characteristics on sunlight-driven NTO photolysis efficiency. The protonated TA-COFs significantly accelerated the photolysis rate, leading to the complete breakdown of NTO within 20 min. This represents the first application of a COF in the catalytic photolysis of NTO.

The results of this research contribute to the ongoing development of reticular design principles, enabling the creation of highly efficient and highly active COF systems tailored for solar energy harvesting and conversion. This progress is facilitated by the exploitation of the distinctive properties inherent to tetrazine units within COF structures. The versatility and performance demonstrated by these materials open up opportunities for expanding the scope of COFs applications in diverse fields and addressing various technological challenges in the future.

Supporting Information

Supporting Information is available from the Wiley Online Library or from the author.

Acknowledgements

This work was supported by the Cornell Center for Materials Research (CCMR) which was supported by the National Science Foundation with grant DMR-1719875. The use of the NMR facility at Cornell University, supported by the NSF through MRI grant number CHE-1531632, is acknowledged. A.S.R. acknowledges support via a Miller Research Fellowship from the Miller Institute for Basic Research in Science, University of California, Berkeley, and computing support from the National Energy Research Scientific Computing Center (NERSC), a U.S. Department of Energy Office of Science User Facility located at Lawrence Berkeley National Laboratory, operated under Contract No. DE-AC02-05CH11231 using NERSC award ERCAP0020225. [Correction added on January 24, 2024, after first online publication: table 1 and table 2 has been updated.]

Conflict of Interest

The authors declare no conflict of interest.

Data Availability Statement

The data that support the findings of this study are available from the corresponding author upon reasonable request.

Keywords

covalent organic framework, photocatalyst, porous materials, sensing, solar energy harvesting, tetrazine

Received: October 22, 2023
Revised: November 29, 2023
Published online: January 7, 2024

[1] L. Candish, K. D. Collins, G. C. Cook, J. J. Douglas, A. Gómez-Suárez, A. Jolit, S. Keess, *Chem. Rev.* **2021**, *122*, 2907.
[2] P. Zhou, I. A. Navid, Y. Ma, Y. Xiao, P. Wang, Z. Ye, B. Zhou, K. Sun, Z. Mi, *Nature* **2023**, *613*, 66.
[3] J. Xiao, T. Hisatomi, K. Domen, *Acc. Chem. Res.* **2023**, *56*, 878.
[4] K. Zhang, K. O. Kirlikovali, R. S. Varma, Z. Jin, H. W Jang, O. K. Farha, M. Shokouhimehr, *ACS Appl. Mater. Interfaces* **2020**, *12*, 27821.
[5] R. Kuriki, T. Ichibha, K. Hongo, D. Lu, R. Maezono, H. Kageyama, O. Ishitani, K. Oka, K. Maeda, *J. Am. Chem. Soc.* **2018**, *140*, 6648.
[6] L. Zhang, J. Zhang, H. Yu, J. Yu, *Adv. Mater.* **2022**, *34*, 2107668.
[7] M. A. Emmanuel, S. G. Bender, C. Bilodeau, J. M. Carceller, J. S. Dehovitz, H. Fu, Y. Liu, B. T. Nicholls, Y. Ouyang, C. G. Page, T. Qiao, F. C. Raps, D. R. Sorigué, S.-Z. Sun, J. Turek-Herman, Y. Ye, A. Rivas-Souchet, J. Cao, T. K. Hyster, *Chem. Rev.* **2023**, *123*, 5459.
[8] O. Dumele, L. Dordevic, H. Sai, T. J. Cotey, M. H Sangji, K. Sato, A. J. Dannenhoffer, S. I. Stupp, *J. Am. Chem. Soc.* **2022**, *144*, 3127.
[9] S. Karak, K. Dey, R. Banerjee, *Adv. Mater.* **2022**, *34*, 2202751.
[10] L. Huang, J. Yang, Y. Zhao, H. Miyata, M. Han, Q. Shuai, Y. Yamauchi, *Chem. Mater.* **2023**, *35*, 2661.
[11] F. Kang, X. Wang, C. Chen, C.-S. Lee, Y. Han, Q. Zhang, *J. Am. Chem. Soc.* **2023**, *145*, 15465.
[12] Y. Shi, J. Yang, F. Gao, Q. Zhang, *ACS Nano* **2023**, *17*, 1879.
[13] W. Zhang, L. Chen, S. Dai, C. Zhao, C. Ma, L. Wei, M. Zhu, S. Y. Chong, H. Yang, L. Liu, Y. Bai, M. Yu, Y. Xu, X.-W. Zhu, Q. Zhu, S. An, R. S. Sprick, M. A. Little, X. Wu, S. Jiang, Y. Wu, Y.-B. Zhang, H. Tian, W.-H. Zhu, A. I. Cooper, *Nature* **2022**, *604*, 72.
[14] L. Chen, L. He, F. Ma, W. Liu, Y. Wang, M. A. Silver, L. Chen, L. Zhu, D. Gui, J. Diwu, Z. Chai, S. Wang, *ACS Appl. Mater. Interfaces* **2018**, *10*, 15364.
[15] L. Ascherl, E. W. Evans, J. Gorman, S. Orsborne, D. Bessinger, T. Bein, R. H. Friend, F. Auras, *J. Am. Chem. Soc.* **2019**, *141*, 15693.
[16] A. F. M. El-Mahdy, A. M. Elewa, S.-W. Huang, H.-H. Chou, S.-W. Kuo, *Adv. Opt. Mater.* **2020**, *8*, 2000641.
[17] Y. Nailwal, A. D. D Wonanke, M. A. Addicoat, S. K. Pal, *Macromolecules* **2021**, *54*, 6595.
[18] J.-Y. Yue, L.-P. Song, X.-L. Ding, Y.-T. Wang, P. Yang, Y. Ma, B. Tang, *Anal. Chem.* **2022**, *94*, 11062.
[19] S. T. Emmerling, J. Maschita, B. V. Lotsch, *J. Am. Chem. Soc.* **2023**, *145*, 7800.
[20] J. Wang, Q. Cao, X.-F. Cheng, W. Ye, J.-H. He, J.-M. Lu, *ACS Sens.* **2022**, *7*, 3782.
[21] X.-R. Ren, B. Bai, Q. Zhang, Q. Hao, Y. Guo, L.-J. Wan, D. Wang, *J. Am. Chem. Soc.* **2022**, *144*, 2488.
[22] S. Wei, F. Zhang, W. Zhang, P. Qiang, K. Yu, X. Fu, D. Wu, S. Bi, F. Zhang, *J. Am. Chem. Soc.* **2019**, *141*, 14272.
[23] X. Zhuang, W. Zhao, F. Zhang, Y. Cao, F. Liu, S. Bi, X. Feng, *Polym. Chem.* **2016**, *7*, 4176.
[24] S. Bi, C. Yang, W. Zhang, J. Xu, L. Liu, D. Wu, X. Wang, Y. Han, Q. Liang, F. Zhang, *Nat. Commun.* **2019**, *10*, 2467.
[25] E. Jin, M. Asada, Q. Xu, S. Dalapati, M. A. Addicoat, M. A. Brady, H. Xu, T. Nakamura, T. Heine, Q. Chen, D. Jiang, *Science* **2017**, *357*, 673.
[26] S. Xu, M. Richter, X. Feng, *Acc. Mater. Res.* **2021**, *2*, 252.

[27] J. Yang, F. Kang, X. Wang, Q. Zhang, *Mater. Horiz.* **2022**, *9*, 121.
[28] Y. Xia, W. Zhang, S. Yang, L. Wang, G. Yu, *Adv. Mater.* **2023**, *35*, 2301190.
[29] Z. Zhao, D. Zheng, M. Guo, J. Yu, S. Zhang, Z. Zhang, Y. Chen, *Angew. Chem., Int. Ed.* **2022**, *61*, 202200261.
[30] T. Wang, Y. Zhang, Z. Wang, Y. Chen, P. Cheng, Z. Zhang, *Dalton Trans.* **2023**, *52*, 15178.
[31] P. She, Y. Qin, X. Wang, Q. Zhang, *Adv. Mater.* **2022**, *34*, 2101175.
[32] A. Acharjya, P. Pachfule, J. Roeser, F.-J. Schmitt, A. Thomas, *Angew. Chem., Int. Ed.* **2019**, *58*, 14865.
[33] H.-L. Qian, C. Dai, C.-X. Yang, X.-P. Yan, *ACS Appl. Mater. Interfaces* **2017**, *9*, 24999.
[34] J. Xu, C. Yang, S. Bi, W. Wang, Y. He, D. Wu, Q. Liang, X. Wang, F. Zhang, *Angew. Chem.* **2020**, *132*, 24053.
[35] T. Zhou, L. Wang, X. Huang, J. Unruangsri, H. Zhang, R. Wang, Q. Song, Q. Yang, W. Li, C. Wang, K. Takahashi, H. Xu, J. Guo, *Nat. Commun.* **2021**, *12*, 3934.
[36] S. Xu, H. Sun, M. Addicoat, B. P. Biswal, F. He, S. Park, S. Paasch, T. Zhang, W. Sheng, E. Brunner, Y. Hou, M. Richter, X. Feng, *Adv. Mater.* **2021**, *33*, 2006274.
[37] T. He, Z. Zhao, R. Liu, X. Liu, B. Ni, Y. Wei, Y. Wu, W. Yuan, H. Peng, Z. Jiang, Y. Zhao, *J. Am. Chem. Soc.* **2023**, *145*, 6057.
[38] A. F. M. El-Mahdy, M.-Y. Lai, S.-W. Kuo, *J. Mater. Chem. C* **2020**, *8*, 9520.
[39] A. K. Rappe, C. J. Casewit, K. S. Colwell, W. A. Goddard, W. M. Skiff, *J. Am. Chem. Soc.* **1992**, *114*, 10024.
[40] J. P. Perdew, K. Burke, M. Ernzerhof, *Phys. Rev. Lett.* **1996**, *77*, 3865.
[41] S. Grimme, J. Antony, S. Ehrlich, H. Krieg, *J. Chem. Phys.* **2010**, *132*, 154104.
[42] S. Grimme, S. Ehrlich, L. Goerigk, *J. Comput. Chem.* **2011**, *32*, 1456.
[43] C. Yuan, X. Wu, R. Gao, X. Han, Y. Liu, Y. Long, Y. Cui, *J. Am. Chem. Soc.* **2019**, *141*, 20187.
[44] S. Zhang, G. Cheng, L. Guo, N. Wang, B. Tan, S. Jin, *Angew. Chem., Int. Ed.* **2020**, *59*, 6007.
[45] Y. Li, J. Sui, L.-S. Cui, H.-L. Jiang, *J. Am. Chem. Soc.* **2023**, *145*, 1359.
[46] D. Wu, Q. Che, H. He, M. E. El-Khouly, S. Huang, X. Zhuang, B. Zhang, Y. Chen, *ACS Mater. Lett.* **2023**, *5*, 874.
[47] E. Hamzehpoor, C. Ruchlin, Y. Tao, C.-H. Liu, H. M. Titi, D. F. Perepichka, *Nat. Chem.* **2023**, *15*, 83.
[48] S. Wang, X. Jing, Y. Wang, J. Si, *Polym. Degrad. Stab.* **2014**, *99*, 1.
[49] J. Zhang, M. Zhang, R.-Q. Sun, X. Wang, *Angew. Chem.* **2012**, *124*, 10292.
[50] P. J. Shannon, W. M. Gibbons, S. T. Sun, *Nature* **1994**, *368*, 532.
[51] R. Luo, H. Lv, Q. Liao, N. Wang, J. Yang, Y. Li, K. Xi, X. Wu, H. Ju, J. Lei, *Nat. Commun.* **2021**, *12*, 6808.
[52] H.-T. Feng, J. Zeng, P.-A. Yin, X.-D. Wang, Q. Peng, Z. Zhao, J. W. Y. Lam, B. Z. Tang, *Nat. Commun.* **2020**, *11*, 2617.
[53] S. Ramírez-Barroso, F. Romeo-Gella, J. M. Fernández-García, S. Feng, L. Martínez-Fernández, D. García-Fresnadillo, I. Corral, N. Martín, R. Wannemacher, *Adv. Mater.* **2023**, *35*, 2212064.
[54] Z. Xu, Y. He, H. Shi, Z. An, *SmartMat* **2023**, *4*, e1139.
[55] Y. Xie, Y. Ge, Q. Peng, C. Li, Q. Li, Z. Li, *Adv. Mater.* **2017**, *29*, 1606829.
[56] R. R. Lunt, J. B. Benziger, S. R. Forrest, *Adv. Mater.* **2010**, *22*, 1233.
[57] M. O'neill, S. M. Kelly, *Adv. Mater.* **2011**, *23*, 566.
[58] L. Zhang, L. Yi, Z.-J. Sun, H. Deng, *Aggregate* **2021**, *2*, e24.
[59] H. Li, H. Li, Q. Dai, H. Li, J.-L. Brédas, *Adv. Theory Simul.* **2018**, *1*, 1700015.
[60] L. M. Lanni, R. W Tilford, M. Bharathy, J. J. Lavigne, *J. Am. Chem. Soc.* **2011**, *133*, 13975.
[61] B. J. Smith, W. R. Dichtel, *J. Am. Chem. Soc.* **2014**, *136*, 8783.
[62] L. Grunenberg, G. Savasci, M. W. Terban, V. Duppel, I. Moudrakovski, M. Etter, R. E. Dinnebier, C. Ochsenfeld, B. V. Lotsch, *J. Am. Chem. Soc.* **2021**, *143*, 3430.
[63] A. L. Mcgaughey, P. Karandikar, M. Gupta, A. E. Childress, *ACS Appl. Polym. Mater.* **2020**, *2*, 1256.
[64] R. E. Trifonov, V. Y. Zubarev, A. A. Malin, V. A. Ostrovskii, *Chem* **1998**, *34*, 111.
[65] W. F. Jager, T. S. Hammink, O. Van Den Berg, F. C. Grozema, *J. Org. Chem.* **2010**, *75*, 2169.
[66] G. Haberhauer, R. Gleiter, C. Burkhart, *Chem. - Eur. J.* **2016**, *22*, 971.
[67] F. Mikes, H. Morawetz, D. Vyprachticky, *Macromolecules* **1993**, *26*, 7064.
[68] N. Zhao, J. W. Y. Lam, H. H. Y. Sung, H. M. Su, I. D. Williams, K. S. Wong, B. Z. Tang, *Chem. - Eur. J.* **2014**, *20*, 133.
[69] B. Luo, Y. Zhang, Y. Chen, J. Huo, *Mater. Adv.* **2022**, *3*, 4699.
[70] P.-F. Wei, M.-Z. Qi, Z.-P. Wang, S.-Y. Ding, W. Yu, Q. Liu, L.-K. Wang, H.-Z. Wang, W.-K. An, W. Wang, *J. Am. Chem. Soc.* **2018**, *140*, 4623.
[71] S. Bi, P. Thiruvengadam, S. Wei, W. Zhang, F. Zhang, L. Gao, J. Xu, D. Wu, J.-S. Chen, F. Zhang, *J. Am. Chem. Soc.* **2020**, *142*, 11893.
[72] G. Clavier, P. Audebert, *Chem. Rev.* **2010**, *110*, 3299.
[73] Z. Li, J. Ding, N. Song, J. Lu, Y. Tao, *J. Am. Chem. Soc.* **2010**, *132*, 13160.
[74] X. Yan, H. Liu, Y. Li, W. Chen, T. Zhang, Z. Zhao, G. Xing, L. Chen, *Macromolecules* **2019**, *52*, 7977.
[75] P. Kohls, D. Jadhav, G. Pandey, O. Reiser, *Org. Lett.* **2012**, *14*, 672.
[76] L. Ruiz Espelt, E. M. Wiensch, T. P. Yoon, *J. Org. Chem.* **2013**, *78*, 4107.
[77] T. Xu, W. Lu, X.-F. Wu, W. Chen, *J. Catal.* **2019**, *378*, 63.
[78] Y.-Q. Zou, J.-R. Chen, X.-P. Liu, L.-Q. Lu, R. L. Davis, K. A. Jørgensen, W.-J. Xiao, *Angew. Chem., Int. Ed.* **2012**, *51*, 784.
[79] T. Jabs, R. A. Dietrich, J. L. Dangl, *Science* **1996**, *273*, 1853.
[80] B. H. J. Bielski, G. G. Shiue, S. Bajuk, *J. Phys. Chem.* **1980**, *84*, 830.
[81] J. A. Johnson, J. Luo, X. Zhang, Y.-S. Chen, M. D. Morton, E. Echeverría, F. E. Torres, J. Zhang, *ACS Catal.* **2015**, *5*, 5283.
[82] A. K. Simlandy, B. Bhattacharyya, A. Pandey, S. Mukherjee, *ACS Catal.* **2018**, *8*, 5206.
[83] F. Lima, U. K. Sharma, L. Grunenberg, D. Saha, S. Johannsen, J. Sedelmeier, E. V. Van Der Eycken, S. V. Ley, *Angew. Chem., Int. Ed.* **2017**, *56*, 15136.
[84] N. F. Mott, *Proc. R. Soc. London, Ser. A* **1939**, *171*, 27.
[85] H. E. Katz, A. J. Lovinger, J. Johnson, C. Kloc, T. Siegrist, W. Li, Y.-Y. Lin, A. Dodabalapur, *Nature* **2000**, *404*, 478.
[86] Q. Zhou, P. Audebert, G. Clavier, R. Méallet-Renault, F. Miomandre, Z. Shaukat, T.-T. Vu, J. Tang, *J. Phys. Chem. C* **2011**, *115*, 21899.
[87] K. Gelderman, L. Lee, S. W. Donne, *J. Chem. Educ.* **2007**, *84*, 685.
[88] H. Adenusi, G. A. Chass, S. Passerini, K. V. Tian, G. Chen, *Adv. Energy Mater.* **2023**, *13*, 2203307.
[89] A. Hankin, F. E. Bedoya-Lora, J. C. Alexander, A. Regoutz, G. H. Kelsall, *J. Mater. Chem. A* **2019**, *7*, 26162.
[90] L. F. Schneemeyer, M. S. Wrighton, *J. Am. Chem. Soc.* **1979**, *101*, 6496.
[91] H. Yang, R. Zhao, Z. Lu, L. Xiao, L. Hou, *ACS Catal.* **2023**, *13*, 2948.
[92] N. A. Romero, D. A. Nicewicz, *Chem. Rev.* **2016**, *116*, 10075.
[93] Y. Hou, Z. Wen, S. Cui, X. Guo, J. Chen, *Adv. Mater.* **2013**, *25*, 6291.
[94] H. Chen, C. Liu, M. Wang, C. Zhang, N. Luo, Y. Wang, H. Abroshan, G. Li, F. Wang, *ACS Catal.* **2017**, *7*, 3632.
[95] K. Zhang, G. Lu, F. Chu, X. Huang, *Catal. Sci. Technol.* **2021**, *11*, 7060.
[96] H. Li, W. Chen, Z. Yuan, Y. Jin, Y. Zhao, P. Ma, J. Niu, J. Wang, *Inorg. Chem.* **2022**, *61*, 9935.
[97] W. Xu, J. J. Pignatello, W. A. Mitch, *Environ. Sci. Technol.* **2013**, *47*, 7129.
[98] V. K. Balakrishnan, A. Halasz, J. Hawari, *Environ. Sci. Technol.* **2003**, *37*, 1838.
[99] A. J. Kennedy, A. R. Poda, N. L. Melby, L. C. Moores, S. M. Jordan, K. A. Gust, A. J. Bednar, *Environ. Toxicol. Chem.* **2017**, *36*, 2050.

[100] A. Halasz, J. Hawari, N. N. Perreault, *Environ. Sci. Technol.* **2018**, *52*, 589.
[101] O. Menezes, C. Owens, E. E. Rios-Valenciana, R. Sierra-Alvarez, J. A. Field, J. C. Spain, *Biotechnol. Bioeng.* **2022**, *119*, 2437.
[102] L. Le Campion, C. Giannotti, J. Ouazzani, *Chemosphere* **1999**, *38*, 1561.
[103] A. Terracciano, C. Christodoulatos, A. Koutsospyros, Z. Zheng, T.-L. Su, B. Smolinski, P. Arienti, X. Meng, *Chem. Eng. J.* **2018**, *354*, 481.
[104] L. K. Sviatenko, L. Gorb, J. Leszczynski, *J. Phys. Chem. A* **2023**, *127*, 2688.
[105] A. V. Polezhaev, N. A. Maciulis, C.-H. Chen, M. Pink, R. L. Lord, K. G. Caulton, *Chem. - Eur. J.* **2016**, *22*, 13985.
[106] X. Chen?, X. Huang, Z. Yi, *Chem. - Eur. J.* **2014**, *52*, 17590.
[107] Z. Wang, A. Berbille, Y. Feng, S. Li, L. Zhu, W. Tang, Z. L. Wang, *Nat. Commun.* **2022**, *1*, 130.
[108] N. Saha, A. Sarkar, A. B. Ghosh, A. K. Dutta, G. R. Bhadu, P. Paul, B. Adhikary, *RSC Adv.* **2015**, *5*, 88848.
[109] A. López-Magano, S. Daliran, A. R. Oveisi, R. Mas-Ballesté, A. Dhakshinamoorthy, J. Alemán, H. Garcia, R. Luque, Adv. Mater. 2023, 35, 2209475.
[110] R. Paul, S. Chandra Shit, H. Mandal, J. Rabeah, S. S. Kashyap, Nailwal, Y. Nailwal, D. B. Shinde, Z. Lai, J. Mondal, ACS Appl. Nano Mater. 2021, 4, 11732.
[111] J. A. Menapace, J. E. Marlin, D. R. Bruss, R. V. Dascher, The Journal of Physical Chemistry, 1991, 95, 5509.